

Shark biomimetics: Drag reduction beyond parallel riblets.

Transfer report

Charlie Lloyd : sccjl@leeds.ac.uk

Supervised by

Professor Jeff Peakall, Dr Alan Burns,
Dr Gareth Keevil, and Dr Robert Dorrell.

19th June 2017

Contents

1	Introduction	1
2	Literature Review	2
2.1	Boundary Layers and Skin Friction	3
2.2	Surface Roughness	5
2.3	Riblets	6
2.4	Investigations of the Fluid Dynamics of Shark Scales	9
2.5	Summary	16
3	Research Questions	17
4	Aims and Objectives	18
5	Channel Flow Experiments using Laser Doppler Anemometry	19
5.1	Fundamentals of LDA	19
5.2	Experimental Set Up	21
5.3	Preliminary Results	23
5.3.1	Time Dependence	23
5.3.2	Spatial Dependence of the Velocity Statistics	26
5.4	Conclusions and Further Work	30
6	Replication of a Shark Scale Using Computer Aided Design (CAD)	31
7	Application of Reynolds-Averaged Navier-Stokes to a Periodic Shark Scale Domain	35
7.1	Mathematical Model	35
7.2	Numerical Implementation	36
7.3	Results and Discussion	39
8	Large Eddy Simulation (LES) of a Channel Flow	43
8.1	Mathematical Model	43
8.2	Numerical Implementation	44
8.3	Results and Discussion	46
8.4	Conclusions and Further Work	48
9	6 Month Plan	49
10	High Level Plan	49
11	Publications, Conferences, and Placements	51

References	52
Appendix A: Pressure Coupling Methods	58
Appendix B: The Germano Identity	60

1 Introduction

Dean and Bhushan (2010) define biomimicry as the study of naturally occurring properties of plants and animals for the purpose of inspired design. This particular project investigates how we can reduce the fluid dynamic drag that acts on surfaces, such as ship hulls and aircraft wings, by investigating animals that swim long distances in the ocean. There are several natural mechanisms that have evolved to reduce drag, such as the excretion of mucus, but sharks possess a unique method that can be theoretically replicated and applied to smooth surfaces (Dean and Bhushan, 2010). Sharks have evolved dermal denticles (skin teeth) which help the fish defend against parasites, abrasion, and reduce hydrodynamic drag (Fletcher et al., 2014). While the hydrodynamic benefit of shark scales has been known for decades, most work has been focussed on the riblet features that exist on the crest of some shark scales, examples of which can be observed in Figure 1. These riblets have been simplified and applied to channel flows and aerofoils, typically achieving a maximum drag reduction of $\sim 10\%$ (Discussed in Section 2).

However, riblets are one of many features that are present on shark scales (see Figure 1). Through observation of the surface it is clear that the scales are very three-dimensional and variable in geometry between different shark species and location on the shark (Fletcher, 2015). Some shark species have scales with no riblets, loosely interlocking scales, and variable angles of attack (Fletcher, 2015). It is the variability of shark scales that is the primary focus of this project. Before defining the project research questions, aims, and objectives, the literature concerning riblet and shark scale experiments will be reviewed.

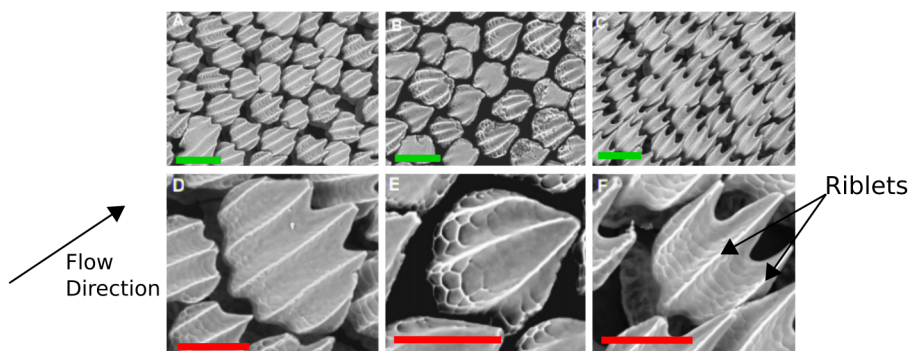


Figure 1: Shark scale samples taken from the head (A, D), the dorsal fin (B, E), and the anal fin (C, F) of a Mako shark. Green scale bars are $200\ \mu\text{m}$; red scale bars are $100\ \mu\text{m}$. Image adapted from Wen et al. (2014).

2 Literature Review

Sharks are the only surviving fishes that possess dermal denticles (Fletcher, 2015). An extensive range of denticles are documented by Reif (1985), highlighting the differences between shark species and the location of scales on the fishes. The study also indicates the complex features of real shark scales such as three dimensionality beneath the exposed scale, overlapping, diverging and converging riblets, variable angles of incidence, and the aerofoil-like shape of each scale with a smooth leading edge and a sharp trailing edge. These features can be observed in Figure 2; even when considering just one species the scales can vary significantly when moving from the head to the tail. Take, for example, the *Scyliorhinus canicula* (demersal ecology) samples in Figure 2; the scales on the head of the shark are tightly interlocking and rounded scales which quickly change to sharp, loosely

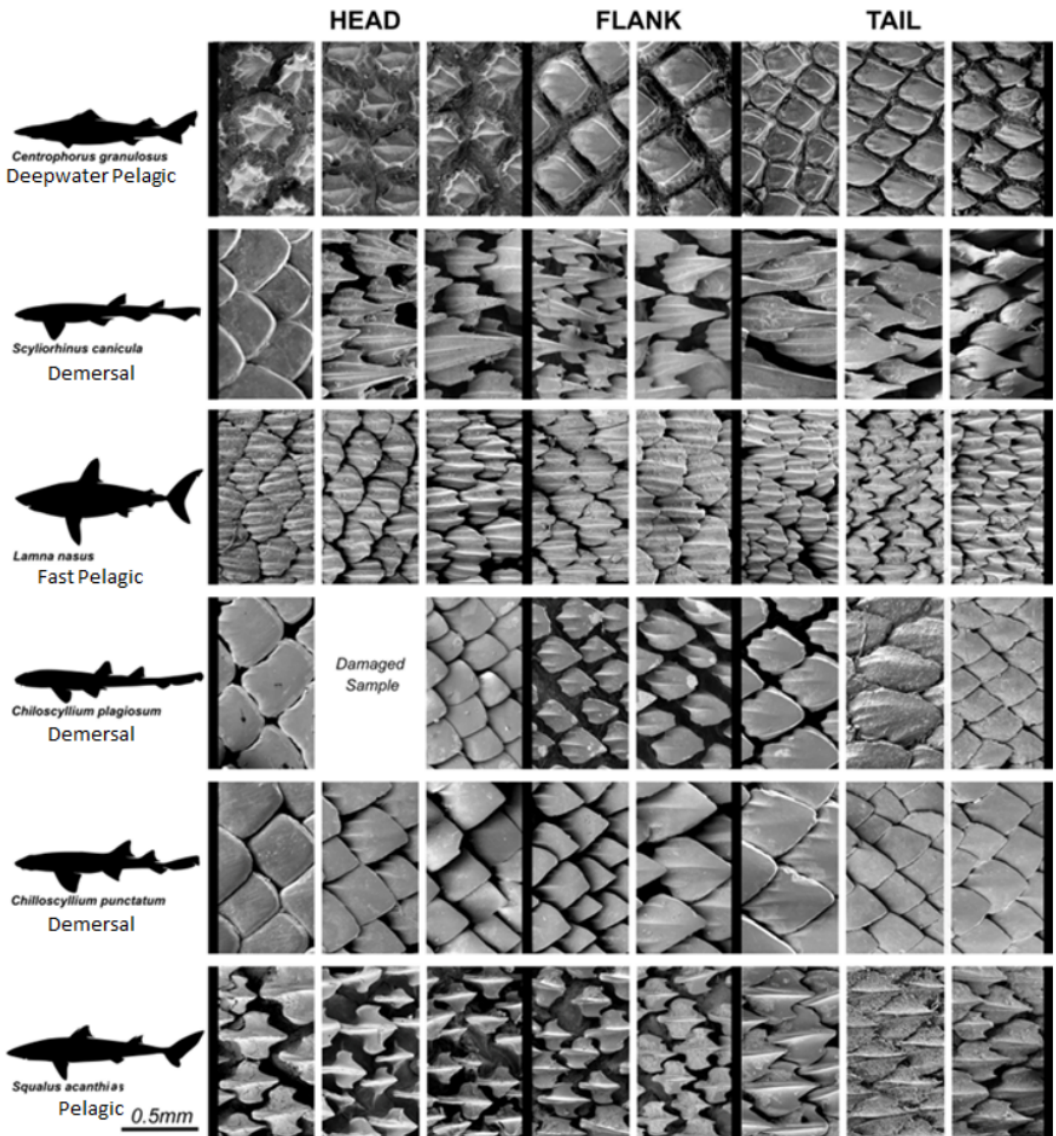


Figure 2: The variation of denticles between six fish species. Image taken from (Fletcher, 2015).

interlocked, and ribletted scales on the shark's flank. The vast range of these features, and the variability between species, results in little understanding as to why many of these features exist. Hydrodynamical aspects have only been studied over the last few decades (Dean and Bhushan, 2010) and have mainly focussed on ripples, examples of which are most prominent on the fast pelagic samples of Figure 2. There has been research into the fluid dynamics of shark scales but there are many gaps and inconsistencies in the literature. These will be discussed in Section 2.4.

2.1 Boundary Layers and Skin Friction

Most engineering and atmospheric flows are bounded by one or many surfaces. These take the form of external flows, such as the flow around cars and aircraft, and internal flows, such as through pipes and channels. Boundary layers are formed as a fluid passes over a surface, whereby the fluid velocity converges to zero as the distance to the wall decreases. Skin friction, arising from the no-slip condition, can be a large contribution to the total drag force that impedes the motion of an object: 50 % of the drag that acts on a ship hull is due to skin-friction (Perlin et al., 2016). A typical boundary layer is presented in Figure 3, which splits the temporally averaged streamwise velocity into several different regions. The velocity and spatial variables are scaled using the fluid kinematic viscosity, ν , and friction velocity, $u_\tau = \sqrt{\tau_w/\rho}$, where τ_w is the wall shear stress and ρ is the fluid density:

$$U^+ = \frac{U}{u_\tau}, \quad y^+ = \frac{u_\tau y}{\nu}. \quad (1)$$

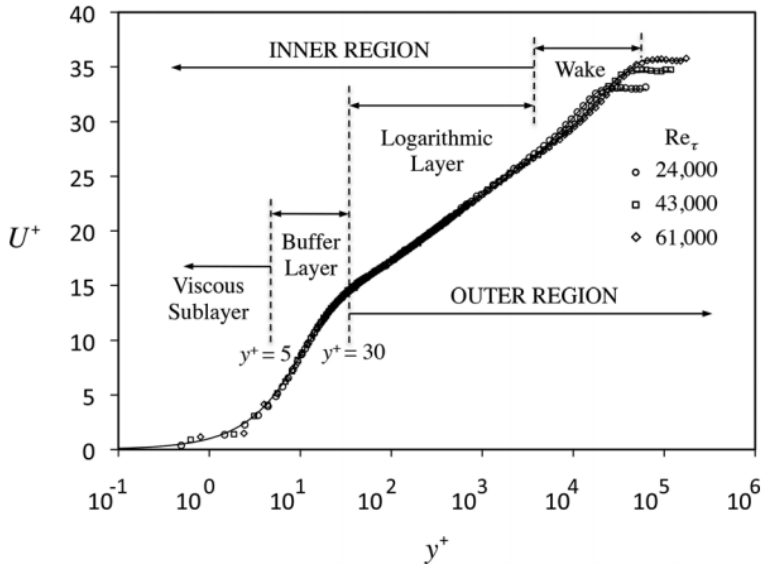


Figure 3: Typical boundary layer profile for three Reynolds numbers. Image taken from Perlin et al. (2016).

By using this scaling the velocity profiles of many external and internal flows behave in the way indicated by Figure 3, whereby the boundary layer is split into external and internal regions. The inner region consists of a viscous sub-layer, a buffer layer, and a logarithmic layer. When in the viscous sub-layer the streamwise (wall-parallel) velocity of a fluid is proportional to the distance away from it, such that $U^+ = y^+$. This extends until $y^+ \approx 5$, at which point the production of turbulent kinetic energy rapidly increases until reaching its maximum in the buffer layer (Perlin et al., 2016). The logarithmic region begins at $y^+ \approx 30$, at which point the streamwise velocity behaves like $U^+ = \kappa^{-1} \ln y^+ + B$ where $\kappa \approx 0.4$ is the von Karman constant and $B \approx 5$ is the intercept parameter (Pope, 2001).

The outer layer blends the logarithmic region into the freestream velocity. The wake region, identified by Figure 3, deviates from the log-law and can cover a large amount of the boundary layer. For an external flow the wake region typically exists for $y/\delta^* > 0.2$ where δ^* is the boundary layer thickness, defined as the point at which the mean streamwise velocity is equal to 99 % of the freestream velocity, U_∞ (Pope, 2001). Surface roughness, including shark scales, has no effect on the wake portion of the outer boundary layer (Flack and Schultz, 2010).

Relationships between the skin friction drag and the flow field can be derived from the Reynolds equations (2) and the continuity equation (3) (Pope, 2001):

$$\frac{\partial \langle U_i \rangle}{\partial t} + \langle U_j \rangle \frac{\partial \langle U_i \rangle}{\partial x_j} = - \frac{\partial \langle P \rangle}{\partial x_i} + \nu \left(\frac{\partial \langle U_j \rangle}{\partial x_i} + \frac{\partial \langle U_i \rangle}{\partial x_j} \right) - \frac{\partial \langle u_i u_j \rangle}{\partial x_i}, \quad (2)$$

and

$$\frac{\partial \langle U_i \rangle}{\partial x_i} = 0, \quad (3)$$

where the three component velocity vector, U_i , and the kinematic pressure, P , are decomposed into an ensemble mean and fluctuating component: $U_i = \langle U_i \rangle + u_i$, and $P = \langle P \rangle + p$. $\langle u_i u_j \rangle$ is termed the Reynolds stresses which account for the effect of velocity fluctuations on the mean flow (Pope, 2001). The FIK identity, named after Fukagata, Iwamoto, and Kasagi, manipulates (4) to determine a relationship for the coefficient of skin friction (Fukagata et al., 2002). For a statistically steady and fully developed channel flow the FIK identity reduces to

$$C_f = \frac{\tau_w}{\frac{1}{2} \rho U_b^2} = \frac{12}{Re_b} + 12 \int_0^\delta 2 \left(1 - \frac{y}{\delta} \right) \left(-\frac{\langle u_x u_y \rangle}{4 U_b^2} \right) dy, \quad (4)$$

where C_f represents the coefficient of friction and Re_b is the bulk Reynolds number based on the bulk velocity, U_b , and the channel half height, δ . Similar equations can also be derived for pipe flows and flat plates. Newhall (2006) derives an integrated boundary layer equation, similar to (4), to compare the skin friction coefficients for smooth and rough flat plate flows.

By setting the Reynolds stresses to zero it is clear that (4) is decomposed into a laminar and turbulent component (Kasagi and Fukagata, 2006). It is the reduction of this turbulent component that is key to how riblets reduce drag, as will be discussed in Section 2.3.

2.2 Surface Roughness

The majority of real engineering problems are subject to surface roughness which generally increases skin friction. The first quantitative study on the effect of surface roughness was carried out by Nikuradse (1933) who applied different grain sizes of sand to a pipe flow and measured the resulting friction factor (equivalent to the coefficient of friction, C_f). Nikuradse (1933) observed that for laminar, and transitional flows, surface roughness had little effect, and its effect on fully turbulent flows was dependent on the relative size of the roughness. To describe the effect of roughness on turbulent flows three regimes were defined, based on the average roughness height, k_s :

$$\frac{k_s u_\tau}{\nu} < 5 : \text{Hydraulically smooth},$$

$$5 \leq \frac{k_s u_\tau}{\nu} \leq 70 : \text{transitionally rough},$$

$$70 < \frac{k_s u_\tau}{\nu} : \text{fully rough}.$$

The hydraulically smooth regime occurs when the roughness elements do not protrude above the viscous sub-layer; in this case roughness has no effect. During the transitional stages roughness elements begin to protrude beyond the viscous sub layer, creating additional turbulent mixing and form drag on individual elements; both of these effects increase the friction factor relative to a smooth surface. The effect of roughness continues to grow until entering the fully-rough regime, at which point the friction factor is no longer a function of the Reynolds number.

In terms of the mean velocity profile, roughness has the effect of shifting the logarithmic layer towards the wall such that the velocity behaves like

$$U^+ = \frac{1}{\kappa} \ln y^+ + B - \Delta U^+, \quad (5)$$

where ΔU^+ represents the shift (Newhall, 2006). The gradient of the logarithmic region remains the same for both smooth and rough surfaces. In addition to this the outer layers of the boundary experience no change when subject to surface roughness, despite there being an increase to the boundary layer thickness, δ^* (Perlin et al., 2016).

2.3 Riblets

An extensive amount of work has been carried out on simplified, sharkskin-inspired, riblets which has been successful in reducing drag for open channel flows, closed channel flows, and when applied to aerofoils (Bixler and Bhushan, 2013). These riblets are generally two-dimensional, whereby there is no variation in cross section in the streamwise direction. The most popular cross sectional shapes are blade-like, sawtooth, and scalloped, although they are theorised to reduce drag in the same way. An example of blade-like riblets is presented in Figure 4, and when compared to the denticle samples of Figure 2 it is clear that the intricate details present on real shark scales are lost. Riblets are typically characterised by their spacing in wall units, $s^+ = u_\tau s / \nu$ (Dean and Bhushan, 2010), although other length scales have been suggested. For example, Garcia-Mayoral and Jimenez (2011) propose a scaling based on the cross-sectional groove area, $(A_g^+)^{1/2}$. The performance of a typical ribletted surface is presented in Figure 5, whereby the difference in wall shear stress, $\Delta\tau/\tau_0$, is plotted against the dimensionless riblet spacing, s^+ . The viscous regime exists for riblets with a spacing of $s^+ \lesssim 15$ whereby the drag reduction scales linearly with spacing. For a small riblet spacing the riblets are submerged in the viscous sub-layer. Realising this, Luchini et al. (1991) used the two-dimensional linear Stokes equations to investigate the flow field. The performance of a particular riblet geometry was found to be related to its virtual origin, whereby the riblet surface can be represented by a flat plate whose origin lies somewhere below the riblet tips. Luchini et al. (1991) determined that the virtual origin of spanwise flow lies deeper in the riblet than for streamwise flow. The difference between these two origins is termed the protrusion height, Δh . Luchini et al. (1991) argued that the larger the protrusion height, the larger the restriction on spanwise flow that could otherwise lead to turbulent mixing above the riblets. This theory is supported by the inhibition of near-wall low speed streaks observed by Chu and Karniadakis (1993), and the study of Yang et al. (2016) who observed a reduced number of sweep and ejection events over a ribletted surface which are known to be large contributors to turbulent mixing (Pope, 2001).

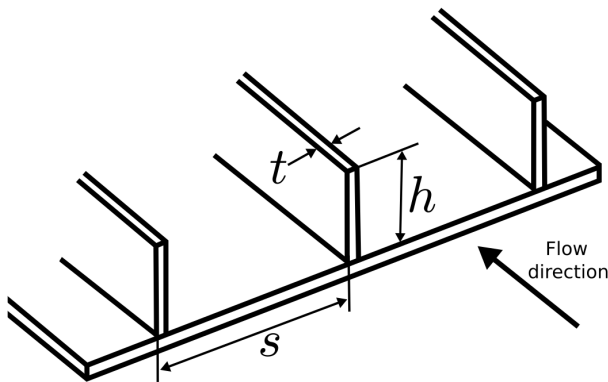


Figure 4: An example of blade-like riblets.

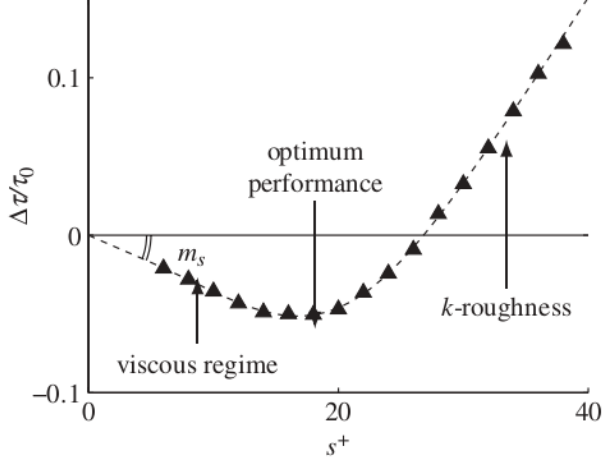


Figure 5: A typical drag reduction profile for a ribletted surface. Image taken from García-Mayoral and Jiménez (2011).

A commonly cited empirical relationship predicting the drag reduction of a ribletted surface was derived by Bechert et al. (1997):

$$\frac{\Delta\tau}{\tau_0} = m_s s^+ = -\frac{\mu_0(\Delta h/s)}{(2C_f)^{-1/2} + (2\kappa)^{-1}} s^+, \quad (6)$$

where m_s is the gradient indicated by Figure 5 and $\mu_0 = 0.785$ is an empirical constant. The roughness parameter of (5) is related to the protrusion height by $\Delta U^+ = -\mu_0 \Delta h^+$, such that the mean velocity profile is shifted away from the wall, contrary to typical rough surfaces. This theory provides a reasonable estimation for the performance of small riblet spacings; through Direct Numerical Simulation (DNS) Garcia-Mayoral and Jimenez (2011) identified a stable spanwise recirculation pattern inside the riblet spacing that mimicked those of a two-dimensional linear Stokes solution. This recirculation pattern became increasingly unstable and asymmetric as the spacing increased. At the optimal region, Garcia-Mayoral and Jimenez (2011) identified the formation of large spanwise vortices, above the riblet tips, due to a Kelvin-Helmholtz type instability. The same vortices were identified in further simulations at a Reynolds number of $Re_\tau = u_\tau \delta / \nu = 550$ (García-Mayoral and Jiménez, 2012). García-Mayoral and Jiménez (2012) also concluded that simulations at low Reynolds numbers of $Re_\tau = 180$, commonly observed in the literature, are equally valid for the study of surface roughness as higher Reynolds numbers, despite perhaps not being as representative of the flow conditions for practical applications.

As the dimensionless riblet spacing increases, the riblets begin to interact with layers above the viscous sub-layer and the predictions of (6) deviate from experiments. The region after the optimum performance behaves like k-roughness, whereby the roughness parameter can be represented by $\Delta U^+ = \kappa^{-1} \ln k_s + A$, where the roughness height, k_s , is related to the dimensions of the riblet (Jimenez, 2004). As the riblet spacing increases,

Table 1: Summary of experimental literature concerning the application of riblets to open channel flows. Adapted from Bixler and Bhushan (2013).

Design	Configuration	Material	Maximum Drag Reduction	Reference
Sawtooth	Continuous	Polymer	8%	(Reidy and Anderson, 1988)
Sawtooth	Continuous	Vinyl	9%	(Rohr et al., 1992)
Sawtooth	Continuous	Vinyl	6%	(Walsh, 1990)
Sawtooth	Continuous	Vinyl	9%	(Neumann and Dinkelacker, 1991)
Blade, Sawtooth & Scalloped	Continuous	Brass	9.9%	(Bechert et al., 1997)
Blade	Staggered & Segmented	Brass	7%	(Bechert et al., 2000)
Blade	Staggered & Segmented	Epoxy	7%	(Bechert et al., 2000)
Blade	Continuous	Titanium & Nickel	4.9%	(Büttner and Schulz, 2011)
Sawtooth	Continuous	Polyurethane	7.6%	(Grüneberger and Hage, 2011)
Blade	Continuous	Metal & Polymer	8.5%	(Wilkinson and Lazos, 1988)
Sawtooth, Scalloped	Continuous	Aluminium & Vinyl	8%	(Walsh, 1982)

they lose their ability to constrict spanwise flow and fast moving fluid can penetrate to the base of the grooves, as observed by Lee and Lee (2001).

The application of riblets to adverse pressure gradients (APG) is still an area of much uncertainty (Boomsma, 2015). Tables 1 and 2 indicate the discrepancies between the application of riblets to channel flows and aerofoils. Even when taking into account the different configurations and riblet types, open channel flow experiments indicate a range of only 5 % for the maximum drag reduction. When riblets are applied to aerofoils the range increases to 10 %. This is largely due to the additional dependencies on riblet configuration and the shape of the foil; the experiments of Chamorro et al. (2013), carried out on a wind turbine blade, indicate that for some cases a partially ribletted foil reduces drag more than a fully covered foil. This is due to development of the boundary layer over the foil; unlike the fully turbulent channel flow experiments the boundary layer of an aerofoil transitions from laminar to turbulent. Uncertainty is further introduced by some

Table 2: Summary of experimental literature concerning the application of riblets on aerofoils. Adapted from Bixler and Bhushan (2013).

Foil Type	Location of Trip (% Chord Length)	Angle of Attack (degrees)	Maximum Drag Reduction	Reference
Symmetric, Thin	No Trip	0	4.3%	Han et al. (2003)
Symmetric, Thin	No Trip	0	13.3%	Caram and Ahmed (1991)
Thin	10%	0-6	6%	Sundaram et al. (1999)
Symmetric	10%	0-6	13%	Sundaram et al. (1996)
Thin	5%	0	14%	Subaschandar et al. (1999)
Thick	No Trip	0	5%	Wetzel and Farokhi (1996)
Thick	No Trip	0	5%	Sareen et al. (2011)
Thick	6%	-0.5-1	10%	Viswanath and Mukund (1995)
Thin	No Trip	0	3.3%	Coustols and Schmitt (1990)
Symmetric, Thin	5%	0	7%	Bixler and Bhushan (2013)

Table 3: Summary of experimental and numerical work concerning the drag reduction properties of shark skin

Scale Type	Replication Method	Experimental Technique	Max Drag Reduction	References
Mako, AOA 10 deg	Printing/casting	Wind tunnel + balance	-13%	Bechert et al. (1985)
Mako, AOA 5 deg	Printing/casting	Wind tunnel + balance	-4%	Bechert et al. (1985)
Silky Shark	Printing/casting	Wind tunnel + balance	-1%	Bechert et al. (1985)
<i>Lophosteus</i>	3D printing	Water flume + LDA	35%*	Fletcher (2015)
<i>Carcharhinus Brachyurus</i>	Moulding	Water flume + balance	12%	Chen et al. (2014)
Not reported	Moulding	Water flume + balance	18.6%	Zhao et al. (2012)
<i>Isurus Oxyrinchus</i>	Moulding	Water flume + balance	8%	Zhang et al. (2011a)
<i>Isurus Oxyrinchus</i> + polymer	Moulding	Water flume + balance	24%	Zhang et al. (2011a)
Not reported	Moulding	Water flume + balance	12%	Luo et al. (2015b)
<i>Carcharhinus leucas</i>	Moulding	Water flume + balance	12%	Luo et al. (2015a)
<i>Carcharhinus leucas</i> + stretched	Moulding	Water flume + balance	14%	Luo et al. (2015a)
Mako	3D printed	Water flume + balance	8.7%	Wen et al. (2014)
Mako	3D printed	Water flume + balance	10%	Wen et al. (2015)
Not reported	Scanned + smoothed	Numerical RANS	13%	Zhang et al. (2011b)
Not reported	Moulding	Water flume + balance	9.5%	Zhang et al. (2011b)
Mako	Scanned + smoothed	Numerical DNS	-50%*	Boomsma (2015)

experiments using a boundary layer trip to shift the transitional point towards the leading edge (see Table 2). There have been more fundamental approaches to the investigation of riblets applied to APG flows; Choi (1990) used a wind tunnel with an adjustable wall height to vary the pressure gradient. It was concluded that the reduction of skin friction is independent of the pressure gradient. In contrast, Nieuwstadt et al. (1993) and Debisschop and Nieuwstadt (1996) measured a drag reduction twice the magnitude of a zero pressure gradient (ZPG) case for an APG case. These results are further supported by the Large Eddy Simulation (LES) of Klumpp et al. (2010) and Boomsma (2015). However, little reasoning behind this increase is given; Boomsma (2015) does provide evidence that the drag reducing mechanisms are the same for both ZPG and APG flows but fails to answer why riblets in an APG are more effective.

2.4 Investigations of the Fluid Dynamics of Shark Scales

There have been very few hydrodynamic experiments carried out on shark scales, and those that have been carried out are rarely in agreement. Table 3 summarises the hydrodynamic experiments that have been carried out on shark scale surfaces applied to channel flows and flat plates. The maximum drag reduction ranges from an increased drag of 50 % to a decreased drag of 35 %. It should be noted that these extreme cases

(highlighted with an asterisk in Table 3) were only carried out at a single flow rate, unlike the other studies. Therefore they are limited to a single calculation of the drag force. The drag reduction of 35 % is associated with the work of Fletcher (2015) who adopted Laser Doppler Anemometry to measure the coefficient of drag for 5 different arrays of fish scales. The scales were 3D printed to a normalised scale length of 2 mm, ensuring that the denticle features were captured to an appropriate resolution. However, no attempt was made to non-dimensionalise the scale width, as opposed to comparable studies on riblets. The use of LDA in this particular case is also questionable: Newhall (2006) validated the use of flow field measurements to calculate the coefficient of drag but suggested that the most accurate method is to measure drag directly, such as through the use of force balances. The advantage of LDA is that flow fields can be resolved, such as the Reynolds stresses, but only the mean velocity profiles are reported by Fletcher (2015). Comparable studies by Wen et al. (2014, 2015) were carried out using mako scales printed at a width of 1.6 mm. The scales in question had riblets on the denticle crown, the spacing of which was used to determine an s^+ value for each flow rate. Drag was directly measured using a force balance and the profile of Figure 6 was obtained. In this case, the difference in drag was quantified by D_s/D_0 rather than $\Delta\tau/\tau_0$, where D_s and D_0 are the drag forces acting on the scales and the reference flat plate respectively. The experiments of Fletcher (2015) were carried out at a bulk velocity of ~ 0.5 m/s. Figure 6 suggests that the drag reducing cases of Fletcher (2015) should be increasing drag by ~ 15 % if the scales behave like those of Wen et al. (2014). It is interesting to note the profiles of Figure 6 when compared to those of the riblets in Figure 5; if the results of Wen et al. (2014) are accurate then the viscous region observed for engineered riblets does not apply to shark scales. Two questions arise from this; how does the drag reduction behave as the riblet spacing reduces further? And is there perhaps a more appropriate length scale other than the riblet spacing? Figure 7 highlights the key dimensions of the mako scale used by Wen et al. (2014). Clearly there are many other length scales that quantify a shark

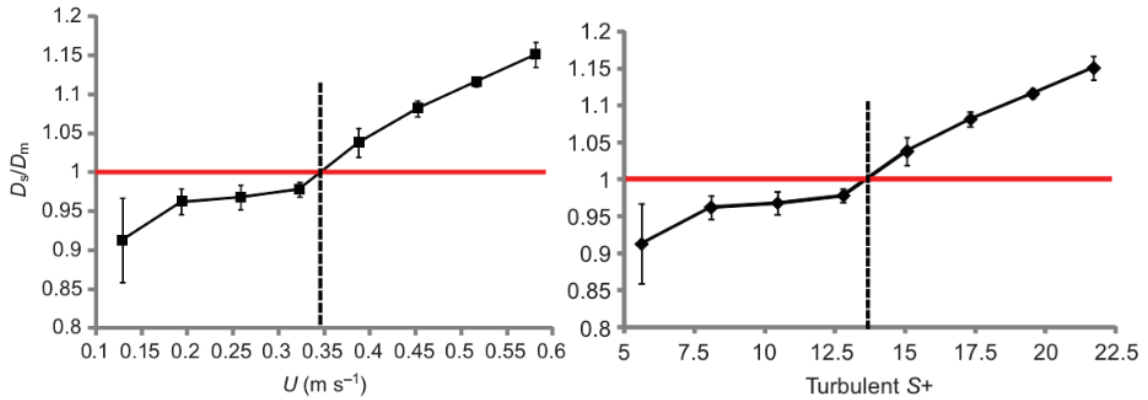


Figure 6: The drag reduction of a denticle array in terms of bulk velocity (left) and dimensionless riblet width (right). Image taken from Wen et al. (2014).

scale. The results of Wen et al. (2014) are further supported by Wen et al. (2015) who investigated the effects of denticle arrangements. Closely interlocked/overlapping scales were found to behave in the way indicated by Figure 6. In contrast, loosely interlocking scales reduced drag for $s^+ \approx 16$ by 3% but increased drag for all over riblet spacings. It might be expected that the optimal riblet spacing for engineered riblets and shark scales would coincide for tightly interlocking scales but these results suggest otherwise. A major limitation noted by Wen et al. (2014) was the pump range of the flume which was unable to operate below a bulk flow velocity of ~ 0.13 m/s. This was also the cause of the large error bars associated with the lowest flow rate, observed in Figure 6. The experiments of Bechert et al. (1985) determined an increased drag, for both mako and silky shark scales, for the full range of s^+ values. However, they did not produce results for $s^+ < 10$ which further supports the argument that smaller denticle riblet spacings need further investigation.

The other extreme result of Table 3 is the DNS of Boomsma (2015). This work adopted an immersed boundary technique to model the flow around the same denticles (staggered and aligned) printed by Wen et al. (2014, 2015), and some engineered riblets. Periodic boundary conditions were adopted to simulate a fully developed channel flow at a Reynolds number of $Re_\tau = 180$ and a riblet spacing of $s^+ = 16$ (for both the engineered riblets and the denticles). The riblet surface behaved as expected; a drag reduction of $\sim 5\%$ was predicted, arising from a reduction of the Reynolds stresses. In contrast, the denticles were found to induce separation and large vortices near the scale surface; both of which contributed to an increase in the Reynolds stresses. The results were validated against those of Bechert et al. (1985) but over predicted the drag compared to Wen et al.

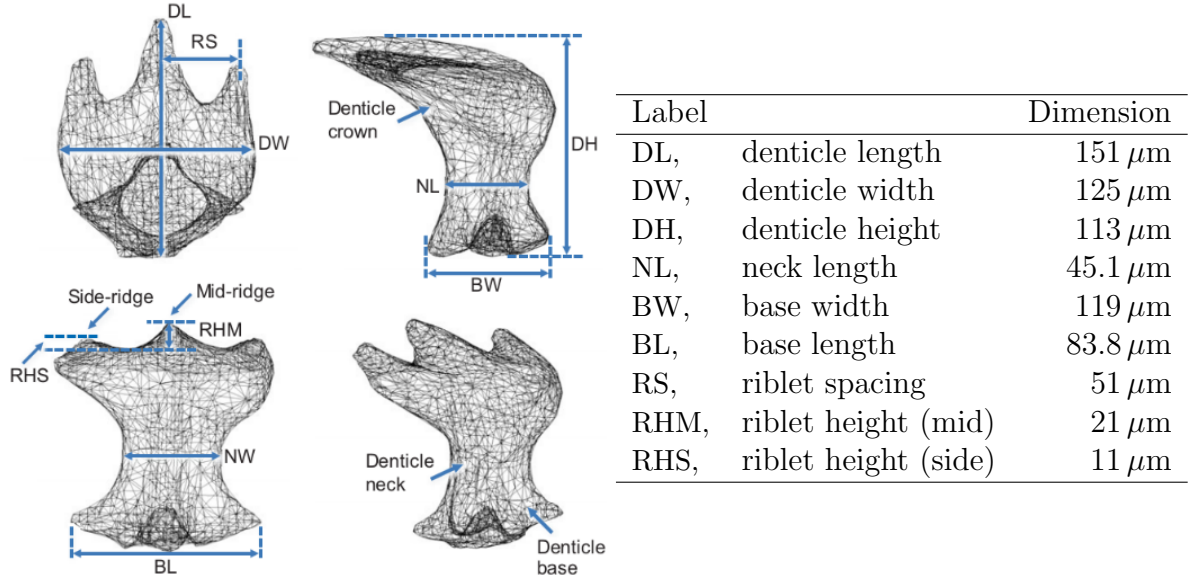


Figure 7: Micro-CT surface mesh of a mako denticle (prior to smoothing and scaling) (left) with corresponding dimensions (right). Image taken from Wen et al. (2014).

(2014, 2015), despite the shark scales being identical. Boomsma and Sotiropoulos (2016) argued that this was due to the different experimental conditions of Wen et al. (2014) and Bechert et al. (1985). The denticles of Wen et al. (2014) were exposed to a developing flow, at a much higher Reynolds number than the simulations. However, the conclusions of García-Mayoral and Jiménez (2012) suggested that, for riblet surfaces, low Reynolds number flows are comparable to high Reynolds number flows, as long as the s^+ values are identical. Boomsma and Sotiropoulos (2016) provide no reason as to why the experiments of Bechert et al. (1985) are in agreement with theirs.

Referring to Table 3 there is still a large spread of drag reduction results, even when ignoring the two extremes. Generally the maximum drag reduction of shark scales is of a greater magnitude than those of engineered riblets, contrary to the results of Bechert et al. (1985). Chen et al. (2014) observed similar drag reduction behaviour for both engineered riblets and ribletted denticles. The denticles consistently outperformed the riblets for the full range of flow rates, achieving a maximum reduction of 12 %. However, no effort was made to relate the bulk velocity to a dimensionless parameter such as s^+ . The denticles were fabricated using a mould which was created from a real shark scale surface. The authors reported a replication error of only 2 % but there are several issues with this technique that are not discussed. Imperfections, asymmetries, and changes in denticle geometry that exist on real shark scale arrays are all captured using the moulding technique. Clearly this model is more physical, but isolating the effects of slight geometric changes between the different denticles is unrealistic using current experimental methods. To the author's knowledge, only tightly interlocking scales have been replicated using this technique (Zhang et al., 2011b,a; Zhao et al., 2012; Chen et al., 2014; Luo et al., 2015a,b). It has yet to be established whether the same methods can be applied to more loosely interlocking scales which are equally common among different shark species (see Figure 2).

A similar technique is adopted by Zhao et al. (2012); a drag reduction of 18% is achieved at the lowest velocity measured, which then reduces to a local minimum, raises to a local maximum, and then reduces to its minimum value at the highest fluid velocity. This result is not discussed, and without support from other literature the validity of the experimental techniques is questionable. Zhang et al. (2011a) adopted the same moulding technology on a *Isurus oxyrinchus* sample. Drag reduction is compared for a ribletted surface, sharkskin replica and a sharkskin replica with non-long polymer chains attached to the surface. The polymer surface was introduced as a method to mimic the mucus excretion of sharks. Small fishes are known to rely on mucus excretion to increase burst swimming speeds; when added to a fluid this mucus can reduce drag by up to 66 % (Fletcher, 2015). However, unlike most fishes, sharks mucus production is restricted to small areas below the denticle crowns. It is therefore often assumed that mucus excretion has a lesser effect for sharks, although the topic is still poorly understood

(Fletcher, 2015). Zhang et al. (2011a) measured a maximum drag reduction of 8% for the sharkskin replica which increases to 24% when the polymer was added. In addition to this, the drag reduction effect increased with increasing flow rate, contrary to the sharkskin without polymer added to its surface. However, Fletcher (2015) suggested that mucus is excreted from pores below the scales. Zhang et al. (2011a) applied the polymer coating to the whole surface, which was perhaps not a physical representation of mucus excretion.

Zhang et al. (2011b) adopted numerical and experimental techniques to investigate the drag reduction of moulded shark scales, although little detail is presented explaining either of the adopted methods. The experimental results indicated a maximum drag reduction of 12.8% at the slowest flow rate, which asymptotes to a value of $\sim 9\%$. This behaviour is similar to that of the non-polymer covered sharkskin of Zhang et al. (2011a), although the magnitude of drag reduction is consistently $\sim 3\%$ higher. The numerical simulations of Zhang et al. (2011b) adopted a finite volume method, with a $k - \epsilon$ turbulence closure, to solve the developing flow field over an array of ~ 30 shark scales. The shark scales were micro-CT scans of those that were replicated. While the model predicted a drag reduction of the same order as the experiments, they increased from 7% to 14% as the flow rate increased; i.e a trend opposite to the experiments. There are several potential causes, such as a lack of grid dependence, convergence, and the use of $k - \epsilon$, which is known to perform poorly in boundary layers (Pope, 2001). However, none of these issues are discussed by Zhang et al. (2011b). Despite this these results are often used to justify the drag reduction observed in experiments (Zhao et al., 2012; Chen et al., 2014).

This section has so far only discussed the literature associated with shark skin applied to flat plates and channel flows. These simple flow configurations are commonly adopted due to their applicability to a wide range of engineering flows, and the repeatability of experiments. This is made clear when referring to the riblet experiments of Section 2.3; channel flows and flat plate experiments agree more closely than when ripples are applied to aerofoils. However, the flow field around a shark is far from the idealised flow in channels. Díez et al. (2015) attempted to resolve the flow around a shortfin mako shark using Computational Fluid Dynamics (CFD). The model adopted the $k - \epsilon$ turbulence closure with wall functions to reduce computing costs. In addition to this, a roughness parameter was used to account for the denticle surface. This is clearly a large simplification to the shark scale geometry but the general flow field around the shark body was captured. The coefficient of drag as a function of position is presented in Figure 8. The results of Díez et al. (2015) indicate a spike in the coefficient of drag near each of the fins and a slowly decreasing coefficient of drag along the main body. The authors also investigated scale morphology, whereby 24 SEM images were taken at various locations on the shark body, although little analysis is provided linking the morphology to the CFD flow field. The authors do note that smooth scales typically

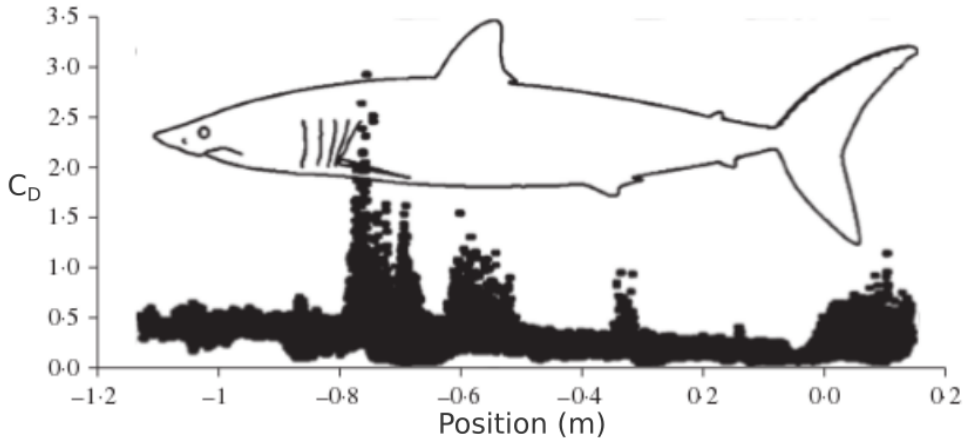


Figure 8: The coefficient of drag distribution over a mako shark. Image taken from Díez et al. (2015).

exist on the leading edge of the fins and the nose of the shark. Riblets are found to be introduced further downstream. One could postulate that since a boundary layer develops from laminar to turbulent, and knowing that surface roughness has no effect in laminar flows (see Section 2.2), the transition from smooth scales to ribletted scales reflects the transition from a laminar to a turbulent boundary layer. However, the same conclusion cannot be drawn when considering the morphological study of Fletcher (2015). Figure 9 displays the contour maps of two denticle geometries over the body of a *Lamna nasus* (Fletcher, 2015). Strongly converging riblets can be observed on the nose and

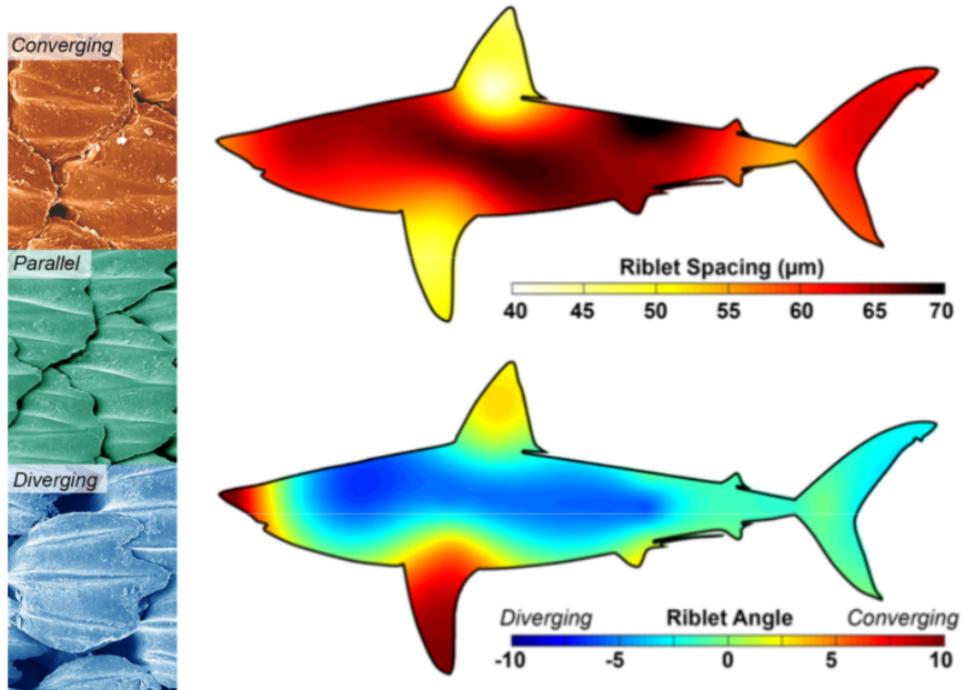


Figure 9: Distributions of riblet spacing and riblet angle for a *Lamna nasus*. Image taken from Fletcher (2015).

pectoral fin of the fish and slightly converging scales are found on the dorsal fin. Fletcher (2015) hypothesised that converging riblets could act as a turbulent trip, similar to those observed on aerofoils (see Section 2.3). This is further supported by the conclusions of Bechert et al. (1985) who argued that denticles could increase turbulent mixing and result in a reduced susceptibility to flow separation. If this is the case then why does the mako shark analysed by Díez et al. (2015) possess smooth scales on the nose? Figure 9 also indicates a reduced riblet spacing on the fins. Referring to Section 2.3 small riblet spacings are associated with higher flow rates; i.e an increase to the friction velocity, u_τ will require a reduction in riblet spacing, s , if the s^+ value is to be maintained. The findings of Díez et al. (2015) reinforce this by determining an increased flow velocity near the fins of the shark.

An aspect of shark skin that has not yet been discussed is the effect of passive bristling as a mechanism for maintaining attached boundary layers. This effect can be observed in Figure 10; while shark scales are rigid, they are embedded into a flexible epidermis which allows the denticle angle of attack to be altered (Lang et al., 2014). The precise mechanism that leads to this bristling is still unknown. Bechert et al. (1985) suggested that the variation in mechanical tension of the epidermis could control the bristling mechanism. At high speeds the epidermis is under larger tension than lower speeds; Bechert et al. (1985) argues that perhaps it is this mechanism that drives scale bristling. However, Lang et al. (2014) concluded that the presence of recirculating flow could be enough to bristle scales alone. This was determined by imaging the effect of a small pulsating jet which created a backflow over a shark skin sample. However, the authors noted that since experiments were carried out on a small section of shark skin the mechanical tension was unlikely to be matched for a real shark. Lang et al. (2014) applied these sharkskin sections to a NACA 4412 aerofoil and measured the resulting flow field using Digital Particle Image Velocimetry (DPIV). They compared the resulting backflow for a sharkskin surface with bristling scales, and a smooth surface. They found that at low

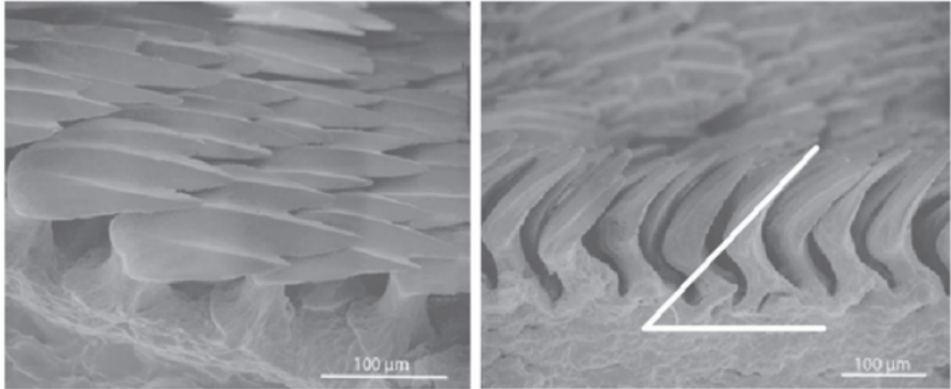


Figure 10: Bristling scales of a shortfin mako. The scales are bristled to an angle of 45° . Image taken from Lang et al. (2014).

angles of attack the sharkskin surface produced more backflow than the smooth surface. However, backflow is substantially reduced for large angles of attack; at a foil angle of 18° there was a large amount of separation for the smooth surface but very little for the sharkskin. The authors hypothesised that at low angles of attack the backflow was too weak to induce bristling, and as a result the performance of the foil was hindered by its increased thickness. However, DPIV is unable to capture the bristling behaviour directly since the scales are so small. There are also other issues with this technique; since sharkskin was directly applied to the foil there is much uncertainty concerning the mechanical properties of the epidermis and the variability between individual scales. These issues are eliminated by the experimental technique of Wen et al. (2014, 2015) who 3D printed an array of smoothed mako scales onto a flexible membrane, mimicking that of a shark epidermis. The membranes are subsequently applied to the surface of a flapping NACA aerofoil, hypothesising that the flexibility of the epidermis could have implications on thrust generation. Both studies concluded that the swimming speed of the flapping foil was increased when denticles were present, but both the cost of transport (energy required per unit distance) and power required increased. The authors suggested that this is likely due to the poor representation of the flexible membrane to real shark skin, where scales are more flexibly embedded into the dermis. It was suggested that dynamic experiments are more representative of shark skin and should be further investigated.

2.5 Summary

This section has reviewed the literature concerning engineered riblets and the experiments concerning shark scales. Several inconsistencies and gaps in the literature can be identified:

- The application of engineered riblets to flat plates and channel flows has been well studied in the literature. However, there are still inconsistencies concerning their application to adverse and favourable pressure gradients.
- There is substantial controversy between the literature associated with the application of shark scales to flat plates and channel flows. This is due to the different experimental techniques, manufacturing methods, denticle geometries, and denticle arrangements.
- While the s^+ scaling is appropriate for riblets, there are many denticle length scales that could also be considered; perhaps a combination of these would be more appropriate when considering the performance of denticles.
- Current experiments on denticles have been unable to investigate the effects of small values of s^+ on a flow. Experiments of Bechert et al. (1985) and Wen et al. (2014,

2015) indicate that drag reduction occurs for denticles at a lower s^+ value than for engineered riblets.

- Most hydrodynamic experiments have considered denticles with riblets, but there are many shark species that possess denticles without riblets. The experiments of Fletcher (2015) suggest there could be a hydrodynamic benefit to denticles without riblets. There are also many other geometrical features that have yet to be investigated, such as the effects of converging/diverging riblets on a flow.
- Some of the most informative studies concerning engineered riblets have adopted numerical methods to investigate the intricate flow fields. Numerical techniques have the advantage of being able to provide insight into how denticles interact with a flow, but only a single DNS paper has been published in this subject area.
- The application of scales to separating flows and adverse pressure gradients has seen little investigation. Studies that have been carried out in this area have focused on large scale fluid structures rather than investigating how the flow interacts with the denticles.
- Dynamic experiments have also been recently introduced, whereby the interactions between the flexible epidermis and the denticles can be investigated. These methods can create more physical models but are currently limited to the observation of large scale structures.
- Mucus excretion is another subject that has seen little investigation in terms of shark skin. Authors have often disregarded its effect, but the work of Zhang et al. (2011a) suggests it could have much larger implications.

3 Research Questions

Section 2 indicated several gaps in the literature concerning shark scales. As a result, several research questions have been proposed:

1. What are the effects of small denticles on a flow? Does a viscous regime exist whereby scales behave like riblets?
2. Is there a more appropriate length scale, other than s^+ , that can better parametrise a denticle?
3. What are the effects of denticle geometry on a flow, such as smooth scales, converging/diverging riblets, and the crowns angle of attack?
4. What are the effects of denticles on the flow field? Experiments to date have mainly adopted force balances, which cannot answer this question.

5. What are the effects of denticles on separating flows?

These questions will be answered using a mixture of experimental and numerical techniques. Questions related to denticle geometry will be answered via LDA experiments, LES, and Reynolds Averaged Navier-Stokes (RANS) simulations. The LDA experiments will measure the effects of smooth, and ribletted, 3D printed denticles on a flat plate. LES will be adopted to investigate the effect of these denticles in a periodic channel flow, and RANS will be used to carry out a parametric analysis. There are advantages and disadvantages associated with each of these methods; LDA is a highly accurate, and non-intrusive, experimental technique, but the flow field surrounding individual scales cannot be captured. On the contrary, LES has the capabilities to resolve the turbulent structures near the scales, but requires too much computing power to carry out lots of different case studies. RANS is more suitable for parameter studies, but requires validation.

In addition to this the project will investigate the effect of applying scales to surfaces subject to separating flows. LES, or RANS, will be applied to a separating flow problem in order to quantify the differences between smooth and shark-skin surfaces. The results will be validated against a laboratory experiment using Particle Image Velocimetry (PIV).

4 Aims and Objectives

There are two aims of this project; to investigate the influence of shark scale geometry on a fully developed flow, and to investigate the impact of scales on separating flows. Both of these aims will primarily concern the flow fields close to/around the scales. These will be achieved through completion of the following objectives:

- Carry out LDA experiments for an array of scales on a flat plate, and compare against the results of a smooth surface.
- Carry out a high resolution LES for the same array of scales and validate against LDA data.
- Validate a parametric RANS code against the LES/LDA data and carry out a parametric analysis on the effect of scale geometry on the fluid flow.
- Design and carry out laboratory (PIV) and numerical experiments (TBC) that can be used to investigate the influence of shark scales on separating flows.

5 Channel Flow Experiments using Laser Doppler Anemometry

As discussed in Section 2, little work has been carried out in analysing the fluid flow around shark scale surfaces; most work has primarily made use of force balances which cannot measure velocity or pressure fields. While previous experiments have successfully measured drag reduction for sharkskin they have not yet investigated the fluid dynamic features that are causing it. For this reason we choose to adopt Laser Doppler Anemometry (LDA) to measure a flat plate boundary layer, with and without shark scales. While a flat plate does not replicate the complex flow fields around a shark, it allows comparison against a wide range of empirical and numerical literature data (in the case of smooth plates), and also ensures the results are applicable to a wide range of surface flows, such as boat hulls and pipe walls. In addition to this, understanding how shark scales behave in simple and controllable configurations will provide comparative data when investigating their effects on separating flows. This section details the preliminary experiments, the aim of which is to validate the experimental method and identify changes that must be made to future designs.

5.1 Fundamentals of LDA

LDA is a non-intrusive method of determining a fluids velocity by measuring the Doppler shift of laser light (Zhang, 2010). There are several key components which can be split into two groups; an optical unit, and a receiving unit. The optical unit generates and transmits a pair of laser beams for each velocity component and focusses them onto a small volume. The two beams create a fringe pattern in the measurement volume, the spacing of which, Δx , is determined by the angle of intersection, α , and the light wavelength, λ . This is demonstrated in Figure 11, whereby a particle of velocity \vec{u}_p , passes through the fringe pattern created by the two beams E_a and E_b . The two beams can be represented by

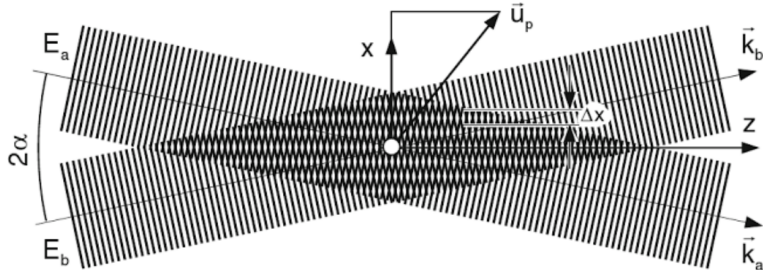


Figure 11: Fringe pattern of an intersecting pair of laser beams. Image taken from Zhang (2010).

$$E_a = E_0 \cos [\omega_a t - k_a(z \cos \alpha - x \sin \alpha)], \quad (7)$$

and

$$E_b = E_0 \cos [\omega_b t - k_b(z \cos \alpha + x \sin \alpha)], \quad (8)$$

where E_0 represents the wave amplitude, ω represents the respective angular frequencies, and $k = 2\pi/\lambda$ represents the angular wavenumber. The wavelength is related to the speed of light by $c = \lambda f$, where c represents the speed of light, and f represents the oscillation frequency. With some manipulation the x -component of the particle velocity is found to be directly related to the fringe spacing, and the shift in oscillation frequency as the particle passes through the fringes (Zhang, 2010). The receiving components detect this change in frequency and converts this to an electrical signal which can be processed. In order to relate the particle velocity to the fluid velocity the flow is seeded with neutrally buoyant particles. It is assumed that these particles do not deviate from the fluid streamlines.

The present work makes use of two-component LDA, whereby two pairs of beams, one at $\lambda = 514\text{ nm}$ (green light) and one at $\lambda = 488\text{ nm}$ (blue light), are transmitted perpendicular to each other. The respective shifts in frequency are separated by the receiving unit in order to produce two velocity components. Particle velocities are only recorded if a shift in frequency is observed by both beam pairs, thus the covariance of the two velocities (Reynolds stresses) can be analysed.

Velocity biasing is a phenomena that must be considered when utilising LDA. Since velocities are only sampled when particles pass through the focal volume, the subsequent time series does not have a regular sampling interval. For this reason, high velocity fluctuations are measured more often than low velocity fluctuations, which results in a bias towards higher velocities when calculating statistics. The correction method detailed by Zhang (2010) is adopted in the present work, whereby the means and standard deviations are normalised by the amount of time a particle resides in the focal volume, τ . The temporal mean of a velocity component u is therefore calculated by

$$\mu_u = \frac{\sum_{i=1}^N u_i \tau_i}{\sum_{i=1}^N \tau_i}, \quad (9)$$

the standard deviation is calculated by

$$\sigma_u^2 = \frac{\sum_{i=1}^N \tau_i (u_i - \mu_u)^2}{\sum_{i=1}^N \tau_i}, \quad (10)$$

and the covariance between the two components of velocity is calculated by

$$\gamma_{u,v} = \frac{\sum_{i=1}^N \tau_i (u_i - \mu_u)(v_i - \mu_v)}{\sum_{i=1}^N \tau_i}. \quad (11)$$

5.2 Experimental Set Up

The experiments are carried out using a flat plate submerged in a recirculating flume (observed in Figure 12). The plate has the dimensions $L \times w \times h = 500 \times 100 \times 10$ (mm), with semi-circular leading and trailing edge cross sections. The volumetric flow rate is controlled by setting the pump frequency. Relating this to a Reynolds number prior to experiments is non-trivial due to the unknown bulk velocity in-between the plate and the flume wall. Subsequently, the Reynolds number is estimated from the measured profiles. The operating range of the pump is 4 Hz to 16 Hz. As discussed in Section 2.4, previous experiments have been unable to capture the effects of sharkskin at small values of s^+ . Experiments are therefore carried out at low pump frequencies of 4 Hz and 8 Hz. A grid is created in order to define the locations at which the velocity is measured. The LDA probe is mounted to a traverse and calibrated such that $(0, 0, 0)$ lies along the centre of the plate at the most upstream point of the flat section. The streamwise coordinate is defined as x and the wall-normal as y . As discussed in Section 2, the viscous sub-layer exists up to $y^+ \approx 5$. If this is to be measured accurately the wall-normal grid size must be of the same order as the wall-unit length scale, $\delta_\nu = u_\tau/\nu$. In addition to this, the location of the wall must be known to the same order. For this reason the wall-normal

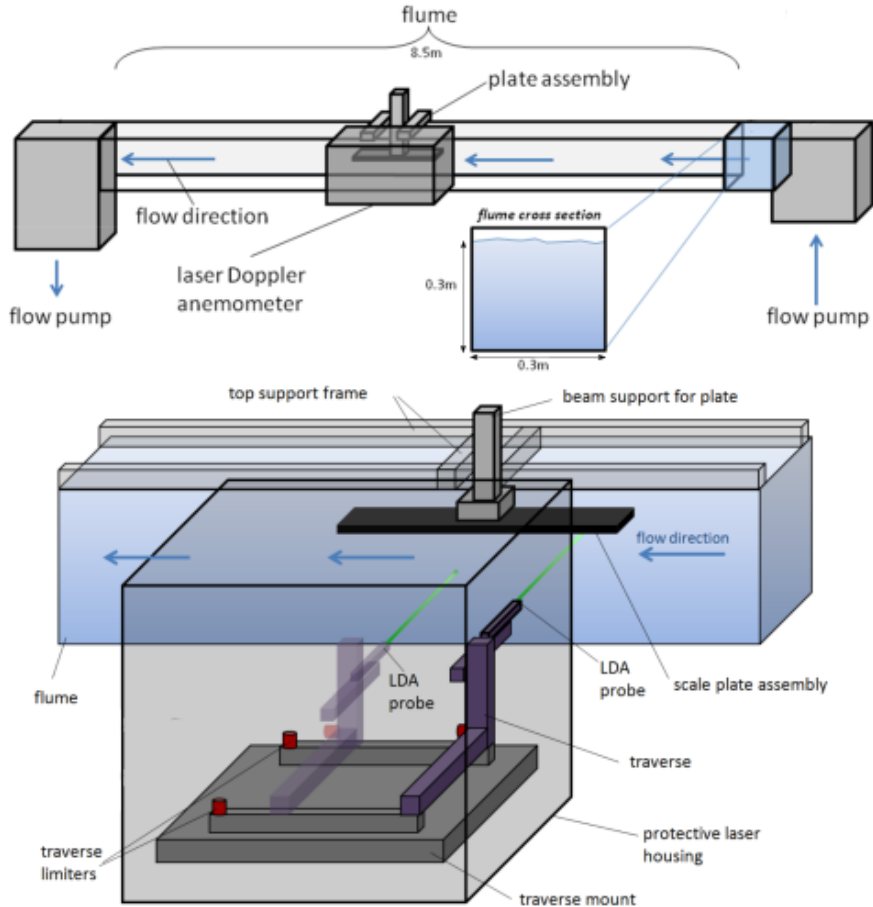


Figure 12: Rig design adapted from Fletcher (2015)

zero position is set to lie in the flat plate, such that the first few wall-normal grid points lie in the wall. This ensures that the full velocity profile can be captured. The following grid is defined such that a high spatial resolution is present near the wall which blends into a low resolution in the far field:

$$\Delta_y = \begin{cases} 0.025, & \text{for } 0 \leq y < 2.5, \\ 0.05, & \text{for } 2.5 \leq y < 3, \\ 0.1, & \text{for } 3 \leq y < 5, \\ 0.5, & \text{for } 5 \leq y < 20, \\ 1, & \text{for } 20 \leq y < 30, \\ 5, & \text{for } 30 \leq y < 75, \end{cases}$$

where the grid spacing, Δ_y , and the wall-normal coordinate, y , are defined in mm. The total number of grid points is 180 which is more than required to capture the profiles accurately. Future experiments will re-evaluate the grid based on the findings of the present study.

The time series measured at each point is passed through a moving average filter in order to remove anomalies. Anomalies are identified if they lie outside the range

$$\mu_{u,2s} - 2\sigma_{u,2s} < u < \mu_{u,2s} + 2\sigma_{u,2s}, \quad (12)$$

where s is half the width of the filter window and u is a component of velocity. $\mu_{u,2s}$ and $\sigma_{u,2s}$ are defined by

$$\mu_{u,2s} = \frac{\sum_{i=-s}^s u_i \tau_i}{\sum_{i=-s}^s \tau_i}, \quad (13)$$

and,

$$\sigma_{u,2s}^2 = \frac{\sum_{i=-s}^s \tau_i (u_i - \mu_{u,2s})^2}{\sum_{i=-s}^s \tau_i}. \quad (14)$$

The anomalies identified by the filter were removed from the data set rather than replaced. In order to calculate the covariance of the two velocity components, any spikes identified in one velocity data set were also removed from the other. Other filters were also tested; a global averaging method was found to remove ‘real’ data due to its inability to differentiate between anomalies and low/high speed structures passing through the probe volume. The filtering method of Goring and Nikora (2002), designed for Acoustic Doppler Anemometry data, was also found to identify more anomalies than expected.

5.3 Preliminary Results

Two sets of results are presented in this section; a time dependence analysis of the means, standard deviations, and the covariance of the two velocity components; and an analysis of the measured profiles. The time dependence study investigates the convergence of statistics as a function of the averaging time. This allows the errors associated with short averaging times to be estimated, and also provides information regarding how much averaging time is required to reduce the error to an acceptable level. The second section investigates the spatial dependency on the flow statistics which will ultimately be used to compare the differences between sharkskin and smooth surfaces.

5.3.1 Time Dependence

Time dependence was assessed at three vertical locations, 400 mm from the upstream end of the plate. These positions were at $y = 1$ mm, 15 mm, and 40 mm. This analysis also investigates how the statistics converge against the number of samples measured. This is dependent on the sampling rate of the LDA, and the local time scale of the flow. It is expected that high local velocities will result in a higher sampling rate.

The probe measured velocities for 300 s at each location for pump speeds of 4 Hz and 8 Hz. The mean streamwise velocity as a function of time is defined as $\mu_u(t)$, whereby μ_u is evaluated between $t = 0$ and t . The standard deviations and covariance are defined using the same notation. Convergence is determined by normalising these quantities against their evaluation over the whole time series. These reference values can be observed in Table 4.

Figures 13 to 17 indicate how the statistics converge as the averaging time, and sample number, increase. For clarity, only the two extreme y positions are plotted. Figure 13 indicates fast convergence for the mean streamwise velocity at $y = 40$ mm for both pump speeds. An averaging window of $\lesssim 30$ s can reduce the error to below 1 %. As expected, the mean streamwise velocity converges more slowly near the wall. After ~ 30 s convergence to ~ 5 % is achieved for the pump frequency of 8 Hz, but only 10 % for

Table 4: Reference values of means, standard deviations, and the covariance of the two velocity components.

Pump Frequency (Hz)	z location (mm)	$\mu_u(300)$ (m/s)	$\mu_v(300)$ (m/s)	$\sigma_u(300)$ (m/s)	$\sigma_v(300)$ (m/s)	$\gamma_{u,v}(300)$ (m^2/s^2)
4	1	0.027081	-0.000173	0.008319	0.000773	-0.000002
4	15	0.091392	-0.000447	0.008947	0.005598	-0.000019
4	40	0.100255	-0.000787	0.008099	0.005211	-0.000011
8	1	0.085152	-0.000843	0.023807	0.003023	-0.000031
8	15	0.185502	-0.001367	0.015663	0.009869	-0.000047
8	40	0.204352	-0.001552	0.013103	0.008496	-0.000027

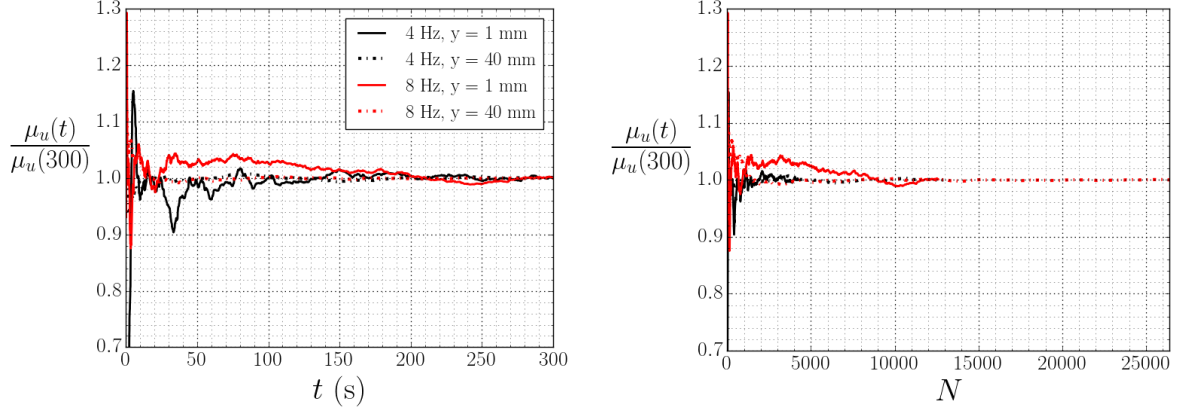


Figure 13: Convergence of the mean streamwise velocity as a function of time (left) and sample number (right).

4 Hz. In order to reduce the low pump frequency error to below 5 % an averaging window of ~ 50 s is required. Both pump frequencies require an averaging window of ~ 200 s to converge to within a ~ 1 % error. In terms of the number of samples, it takes more than twice as many to converge for the higher pump frequency. These results suggest that convergence of the mean streamwise velocity is more dependent on averaging time rather than the number of samples obtained.

Figure 14 indicates very poor convergence for the mean vertical component of velocity, especially for the low pump frequency. This is likely due to the tolerances of the LDA; the recorded wall-normal velocities are of order 0.1 mm/s for the low pump frequency. This is at least two orders of magnitude lower than the streamwise velocity measurements, even close to the wall. For completeness the statistics were not omitted, but the mean wall-normal velocity is rarely published in boundary layer literature.

The standard deviations are important due to their relationship with the turbulent

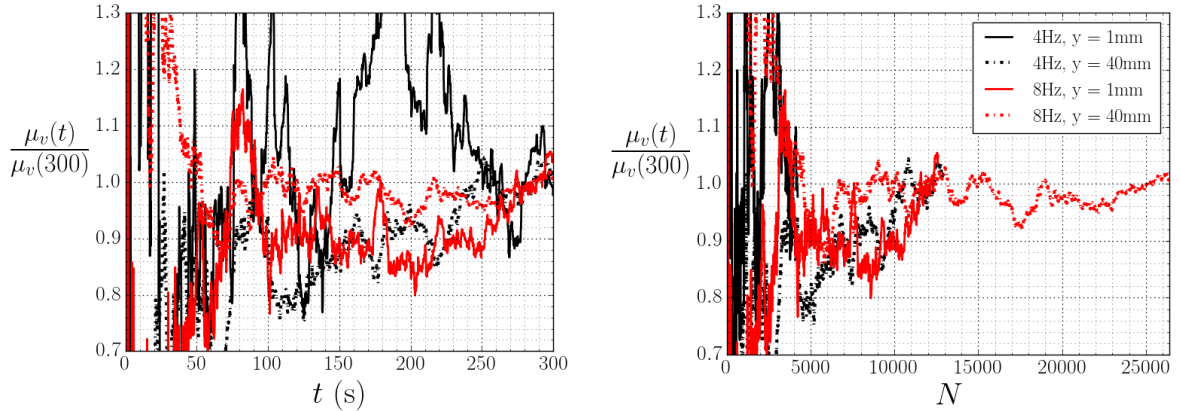


Figure 14: Convergence of the mean wall-normal velocity as a function of time (left) and sample number (right).

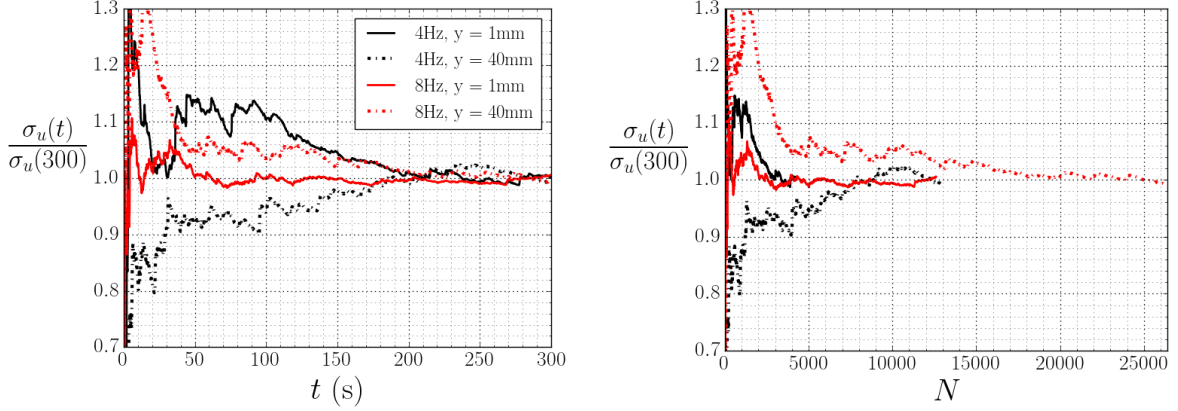


Figure 15: Convergence of the standard deviation of the streamwise velocity as a function of time (left) and sample number (right).

kinetic energy and the Reynolds stresses. As observed in Figure 15, the standard deviations of the streamwise velocity, at a pump frequency of 4 Hz, converge at the same rate for both vertical positions, taking ~ 130 s to reduce to a 5 % error, and ~ 200 s to reduce to 2 %. In contrast, the standard deviation at $y = 1$ mm converges more quickly than at $y = 40$ mm, for the higher pump frequency. This can be explained by referring to Table 4; for a pump frequency of 4 Hz the magnitude of σ_u is of a similar magnitude for both y locations. This is not the case for the higher pump frequency; at $y = 1$ mm the magnitude of σ_u is larger than at $y = 40$ mm, suggesting that convergence is related to the magnitude of the statistic in question. At $y = 1$ mm the standard deviation reduces to an error of ~ 2 % after just 60 s. In contrast, it takes ~ 200 s at $y = 40$ mm. Figure 15 also indicates that convergence is more dependent on the averaging time rather than the number of samples. After ~ 200 s all four profiles have converged within ~ 2 % of their final value, but there is no common sample number that suggests convergence.

The convergence of the wall-normal velocity standard deviations can be observed in Figure 16. After ~ 100 s all four profiles converge at the same rate. An error of ~ 4 % is obtained after 100 s and ~ 2 % after 220 s. Again, convergence appears to be more dependent on the time interval rather than the number of samples.

The covariance of the two velocity components converges very slowly, as indicated by Figure 17. Even after 300 s, only the near wall point for the high pump frequency indicates reasonable convergence, whereby the error is reduced to ~ 2 % after ~ 250 s. Although this estimate makes the assumption that $\gamma_{u,v}(300)$ represents the ‘true’ value. Figure 17 also highlights some sudden jumps in the near wall, low pump speed covariance. This could have arisen from non-physical spikes in the $(u - \mu_u)(v - \mu_v)$ time series. Perhaps the filtering method should be applied to more than just the u and v data sets. However, the other three covariances still predict an error of > 10 % after 200 s of averaging time. Clearly, if the Reynolds stresses are to be used to analyse the effect of shark skin then

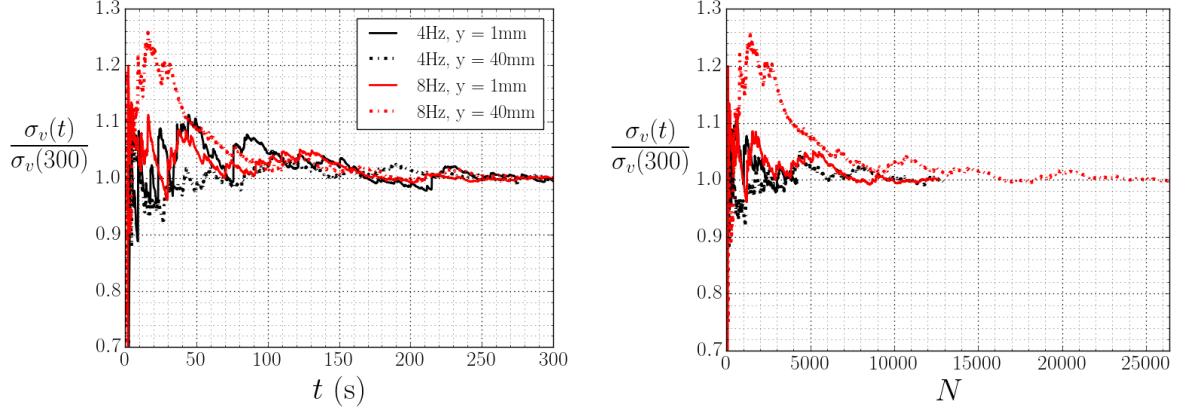


Figure 16: Convergence of the standard deviation of the wall-normal velocity as a function of time (left) and sample number (right).

longer averaging times will be required.

5.3.2 Spatial Dependence of the Velocity Statistics

The means, standard deviations and covariance of velocity are measured along profiles at $x = 300$ mm and $x = 400$ mm. The vertical locations are given in the grid defined in Section 5.2 and profiles are measured for a pump frequency of 4 Hz and 8 Hz. Due to time constraints, velocities were only sampled for 20 s. The errors associated with this are estimated by using the time dependence analysis of Section 5.3.1; the mean streamwise velocity, μ_u , is evaluated over 20 s intervals, throughout the length of the 300 s time series. The mean of the absolute difference between each interval mean and the reference mean, $\mu_u(300)$, is defined as the error. However, since the error can only be estimated at three vertical locations, interpolation is adopted in order to fit the entire profile. Future work will consider many more locations to estimate this error.

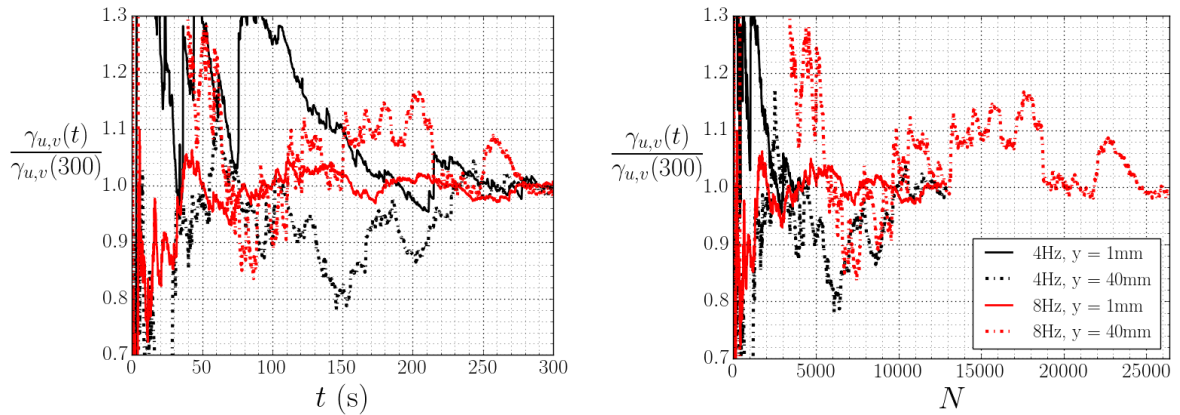


Figure 17: Convergence of the covariance of the streamwise and wall-normal velocities as a function of time (left) and sample number (right).

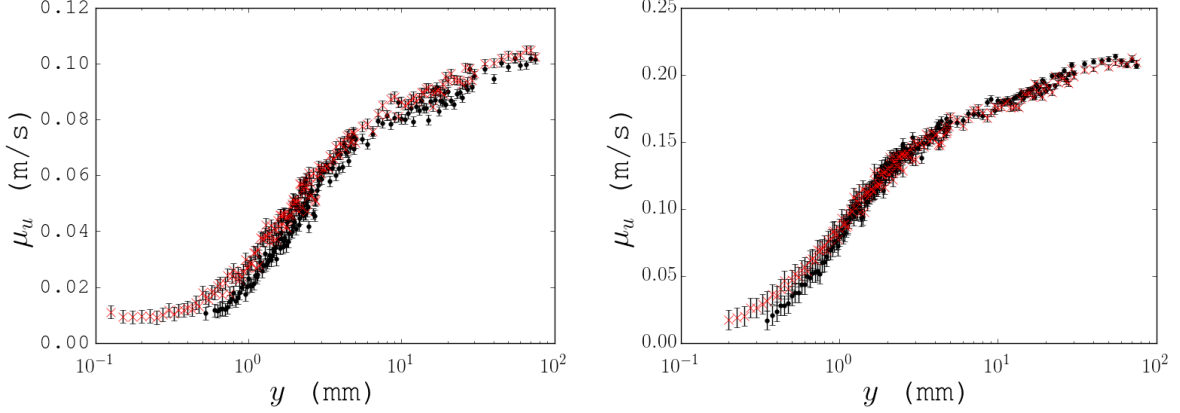


Figure 18: Raw profiles of mean streamwise velocity for pump frequencies of 4 Hz (left), and 8 Hz (right). Symbols represent the following: \bullet , μ_u at $x = 300$ mm; \times , μ_u at $x = 400$ mm.

The mean streamwise velocity profiles can be observed in Figure 18. The logarithmic region of the 8 Hz pump frequency can be distinguished as the linear trend between ~ 2 mm and ~ 20 mm but it is harder to locate for the low pump frequency. This is due to its shorter length and a larger spread in the data, likely due to the short averaging time. However, the viscous and buffer regions are especially well resolved for the mean velocity. Figure 18 also shows a collapse of the $x = 300$ mm and $x = 400$ mm for the higher flow rate, with a small deviation near the wall. This suggests that the velocity profiles are close to fully developed. In contrast, the lower frequency flows indicate a slightly reduced velocity for the entire measured profile. It should be noted that the profiles were only measured up to 75 mm due to experimental constraints. Future experiments will be revised such that half the channel height, $\delta = 100$ mm, can be measured. The low pump frequency results also indicate more points captured in the downstream profile. This suggests that the plate is not quite flat. However, a difference in 0.4 mm over a distance of 100 mm equates to an angle of $\sim 0.3^\circ$ and can therefore be neglected.

The standard deviation profiles can be observed in Figure 19. The wall-normal fluctuations are captured reasonably well for both pump speeds. The two x locations collapse until $y \approx 1$ mm, at which point the wall-normal standard deviations reach their maximum and a larger spread of the data can be observed. At a pump frequency of 8 Hz the streamwise fluctuations reach a maximum in the buffer region. There is a lot of spread in the data, clearly suggesting that longer averaging times are required. Despite the spread in data, a collapse can be observed in the buffer layer, between the two x profiles. These differentiate nearer the wall, indicating that the fluctuations are of a greater magnitude further along the plate. The 4 Hz standard deviations indicate a much larger error in the streamwise direction. The plot also indicates that there is much more spatial resolution between $y = 1$ mm and $y = 3$ mm than is required.

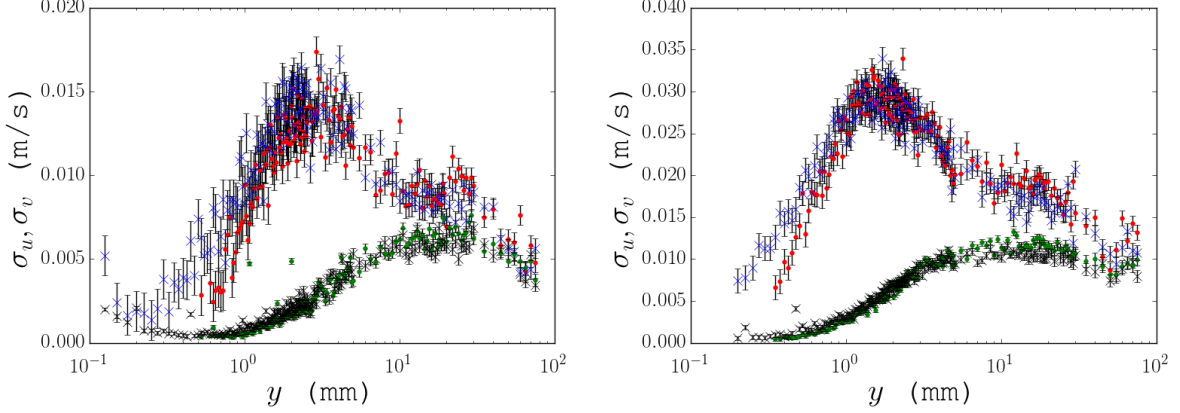


Figure 19: Raw profiles of standard deviations of velocity for pump frequencies of 4 Hz (left), and 8 Hz (right). Symbols represent the following: \bullet , σ_u at $x = 300$ mm; \times , σ_u at $x = 400$ mm; \bullet , σ_v at $x = 300$ mm; \times , σ_v at $x = 400$ mm.

The profiles of velocity covariance can be observed in Figure 20. The covariance indicates a large spread in the data as the distance from the wall increases. The estimated error bars do reflect this increase in uncertainty but the magnitude seems too small in this case. This is likely due to the lack of points used to estimate these errors. It could also be due to the fluctuations in the errors which are not reflected by taking the mean of the absolute error. Future work will investigate the effect of taking into account the standard deviations. It is clear from Figure 20 that if the Reynolds stresses are to be compared between smooth and sharkskin surfaces then a much longer averaging time is required.

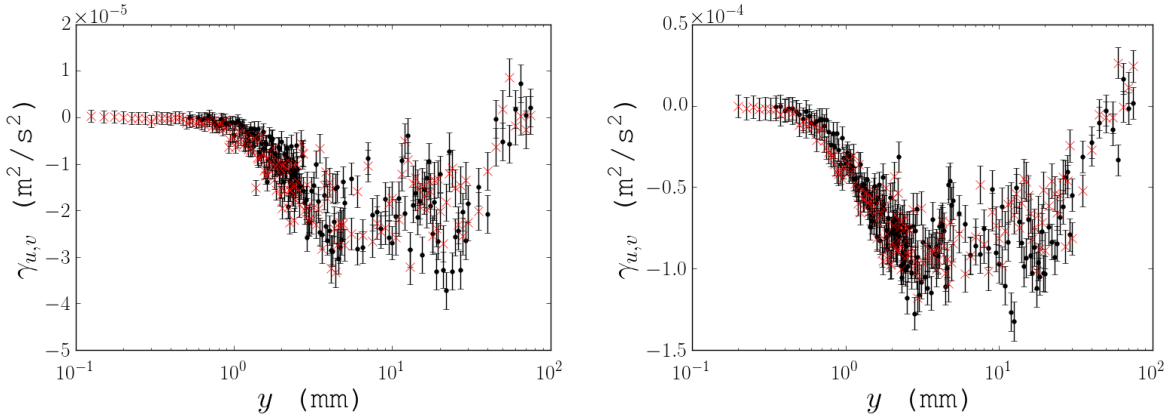


Figure 20: Raw profiles of the covariance of the two velocity components for pump frequencies of 4 Hz (left), and 8 Hz (right). Symbols represent the following: \bullet , $\gamma_{u,v}$ at $x = 300$ mm; \times , $\gamma_{u,v}$ at $x = 400$ mm.

Estimation of the Friction Velocity

In order to compare both smooth and sharkskin surfaces the friction velocity must be estimated from the flow field. There are several methods of doing this, such as using the near wall gradients or using the integrated boundary layer equations of a similar form to (4). The present work adopts the Clauser (1956) method, whereby the logarithmic region identified in Figure 3 is fitted with the empirical equations:

$$U^+ = \begin{cases} y^+, & \text{for } y^+ \lesssim 5, \\ \kappa^{-1} \ln y^+ + B, & \text{for } y^+ \gtrsim 30, \end{cases} \quad (15)$$

where U^+ and y^+ are defined by $U^+ = \mu_u/u_\tau$ and $y^+ = yu_\tau/\nu$. Several challenges are presented with fitting this relationship; the upper bound for the logarithmic layer is dependent on the Reynolds number, and is therefore unknown. In addition to this, the location of the wall has not yet been accounted for in the previous statistics. Subsequently the profile offset needs to be estimated. Since the viscous sub-layer is well resolved, we can estimate the offset by using the equation,

$$y = \mu_u \frac{u_\tau^2}{\nu} + \Delta_w, \quad (16)$$

where Δ_w is the offset from the wall. We adopt least-squares regression to fit the data and subtract Δ_w from the vertical position. The least-squares approach also provides an estimate for u_τ which is subsequently used to estimate the range of vertical positions in the logarithmic region, such that least-squares regression can be applied to

$$\mu_u = \frac{u_\tau}{\kappa} \ln y + \frac{u_\tau}{\kappa} \ln \frac{u_\tau}{\nu} + Bu_\tau. \quad (17)$$

Currently the upper bound of the logarithmic region is defined as $y^+ = 150$ in order to ensure the wake region is not captured. As a result, two estimates of the friction velocity are obtained for each profile, one from (16), and one from (17). These can be observed in Table 5. A maximum difference of 20 % can be observed from the two estimates which is a larger magnitude than would be expected between a smooth and sharkskin surface. The dimensionless velocity profile of the 8 Hz pump frequency, based on the logarithmic

Table 5: Estimates of the friction velocity.

Pump Frequency (Hz)	x location (mm)	u_τ (Viscous estimate) (m/s)	u_τ (log-law estimate) (m/s)	Error (%)
4	300	0.00522	0.00414	20.83
4	400	0.00504	0.00437	13.19
8	300	0.01011	0.00888	12.14
8	400	0.01005	0.00918	08.43

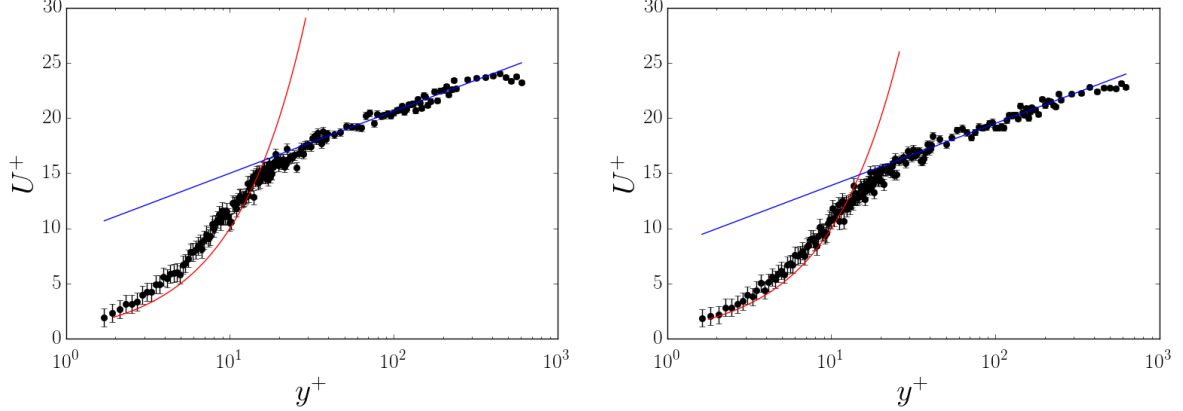


Figure 21: Mean velocity profiles in wall units for a pump frequency of 8 Hz at an x location of 300 mm (left) and 400 mm (right). Red lines represent the estimate of the viscous region, blue lines represent the estimate of the logarithmic region.

estimate of u_τ , is presented in Figure 21. The fit agrees well with the logarithmic region but deviates slightly for the viscous region. The $x = 400$ mm profile indicates that the viscous estimate lies within the error bars of the data, although there is still a difference in u_τ predictions of 8.43 %. Further work will investigate the implementation of this method in an attempt to reduce the error. However, other methods of estimating the friction velocity will also be investigated, such as using the near wall gradients of velocity, and an integrated boundary layer method that takes into account the Reynolds stresses. Of course, the accuracy of the later method is dependent on the resolution of the Reynolds stress profile, which will be a priority in future experiments.

5.4 Conclusions and Further Work

The presented experiments have indicated several adjustments that should be made to the methodology and rig design. The spatial resolution is much higher than required at these low flow rates, especially in the buffer region. In contrast, the averaging time is too short for accurate estimates of the Reynolds stresses, and the standard deviations of velocity. In addition to this, the errors associated with short averaging times have only been estimated at three vertical locations. Future work will carry out experiments on a coarser grid, with longer averaging times, and calculate errors based on more grid points. Furthermore, the methods of estimating u_τ will be re-evaluated before carrying out future experiments. The current work has only investigated means, standard deviations, and the covariance of the two velocity components. However, there are many other methods to quantify turbulent flows. In particular, investigations into energy spectra will provide information regarding the turbulent structures near the wall. In addition to this, quadrant analysis could be adopted in order to identify sweep and ejection events for both smooth and sharkskin surfaces.

6 Replication of a Shark Scale Using Computer Aided Design (CAD)

This section details the process adopted to replicate and simplify a sharks skin denticle, using Computer Aided Design (CAD). The purpose of this work is to create a reference case for future experiments; by varying the parameters of the reference CAD model, the effects of different denticle geometry can be investigated. For this reason, a *Poracanthodes sp.* fish scale (sampled by Fletcher (2015)) was chosen for replication, due to its relatively simple geometry. The 3D *Poracanthodes sp.* model of Fletcher (2015) can be observed in Figure 22. Future models will vary the geometry of the reference scale in order to isolate the effects of different parameters.

There are many features of the scale in Figure 22 that are undesirable for our reference case. In particular, the asymmetries, and the wave-like trailing edge. The reasons for their existence is unknown; perhaps the asymmetries are present to redirect flow, or to interlock better with neighbouring denticles, or perhaps they are random defects that just so happen to be present on the sample that was taken by Fletcher (2015). However, for a reference case a simpler geometry is desired which maintains the main features of the denticle.

The simplified model is defined by fitting a coordinate system to the sample of Figure 22, and taking several cross sections of the scale in the xz -plane. Primitive shapes are used to construct sections that capture the main geometry of the scale, but maintain symmetry and remove complex features. An example of this can be observed in Figure 23. Clearly, the asymmetries and the wave-like features have been removed by the simple cross section. However, this method allows the model to be reduced to 7 parameters for each cross section. These sections are blended together using CREO Parametric software in order to create the 3D model observed in Figure 24. A few discrepancies can be

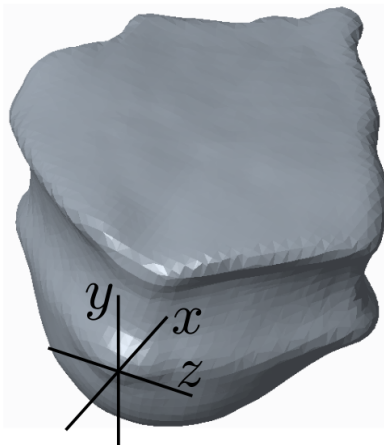


Figure 22: *Poracanthodes sp.* sample from Fletcher (2015). Streamwise direction is positive in x .

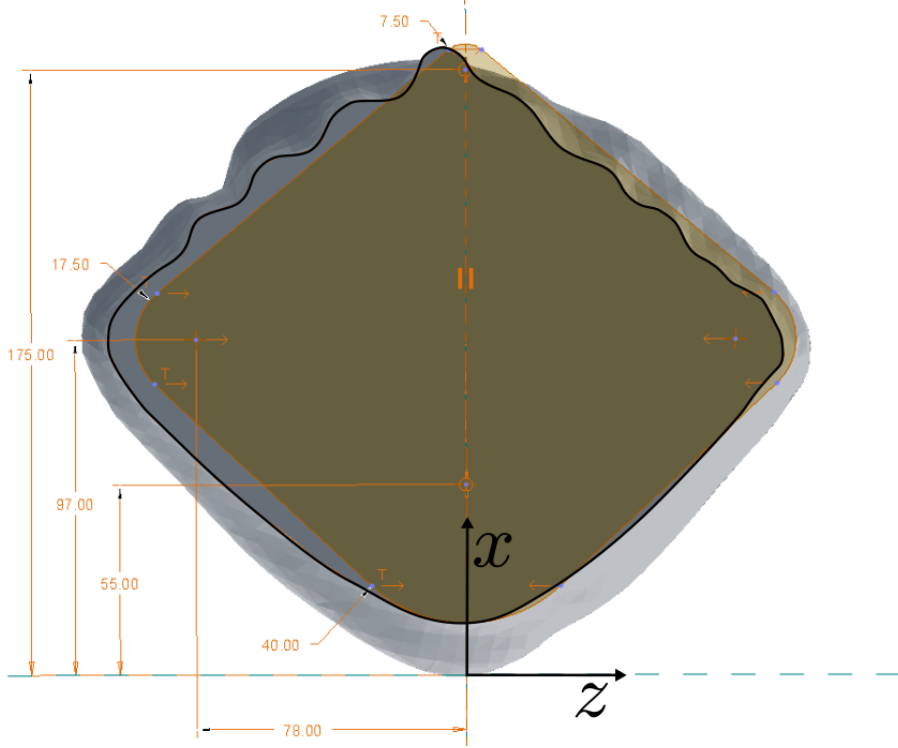


Figure 23: A comparison between a simplified cross section (orange) and the sampled scale cross section (black). The dimensions are scaled after the simplified scale is generated.

observed, but the CAD is adequate for the purpose of a reference model.

Parametric studies can be carried out by varying the parameters specified in Figure 23, although the models response is quite sensitive; small changes can distort the model significantly. For this reason, a systematic approach that varies the parameters using this particular CAD model is unrealistic, due to additional interactions required to ensure model validity. However, there are other, less traditional, CAD methods that can be adopted for this project; Blender, often used for graphical design, is an open source modelling software that allows the creation of organic shapes by manipulating a surface mesh. Blender is also scriptable using python, although the capabilities of this are not yet known. Work alongside the PhD will focus on using Blender as a potential replacement to the current CAD software.

Arrays of the reference CAD model have been 3D printed by the University of Leeds engineering department, and a commercial company, at denticle widths of 1 mm and 2 mm. Since these denticles do not have riblets, it is assumed that the total width is an appropriate length scale. Using the estimations of the friction velocity in Section 5.3.2, these widths correspond to a dimensionless width of $w^+ = u_\tau w / \nu = 3.63$ for the 1 mm width scales, and $w^+ = 7.27$ for the 2 mm width scales, at a pump frequency of 4 Hz. However, the preliminary results have indicated an inadequate resolution, even for the larger scales. A Scanning Electron Microscope (SEM) image of two 2 mm scales can be seen in Figure 25. Poor surface quality can be observed in both images, and the edges

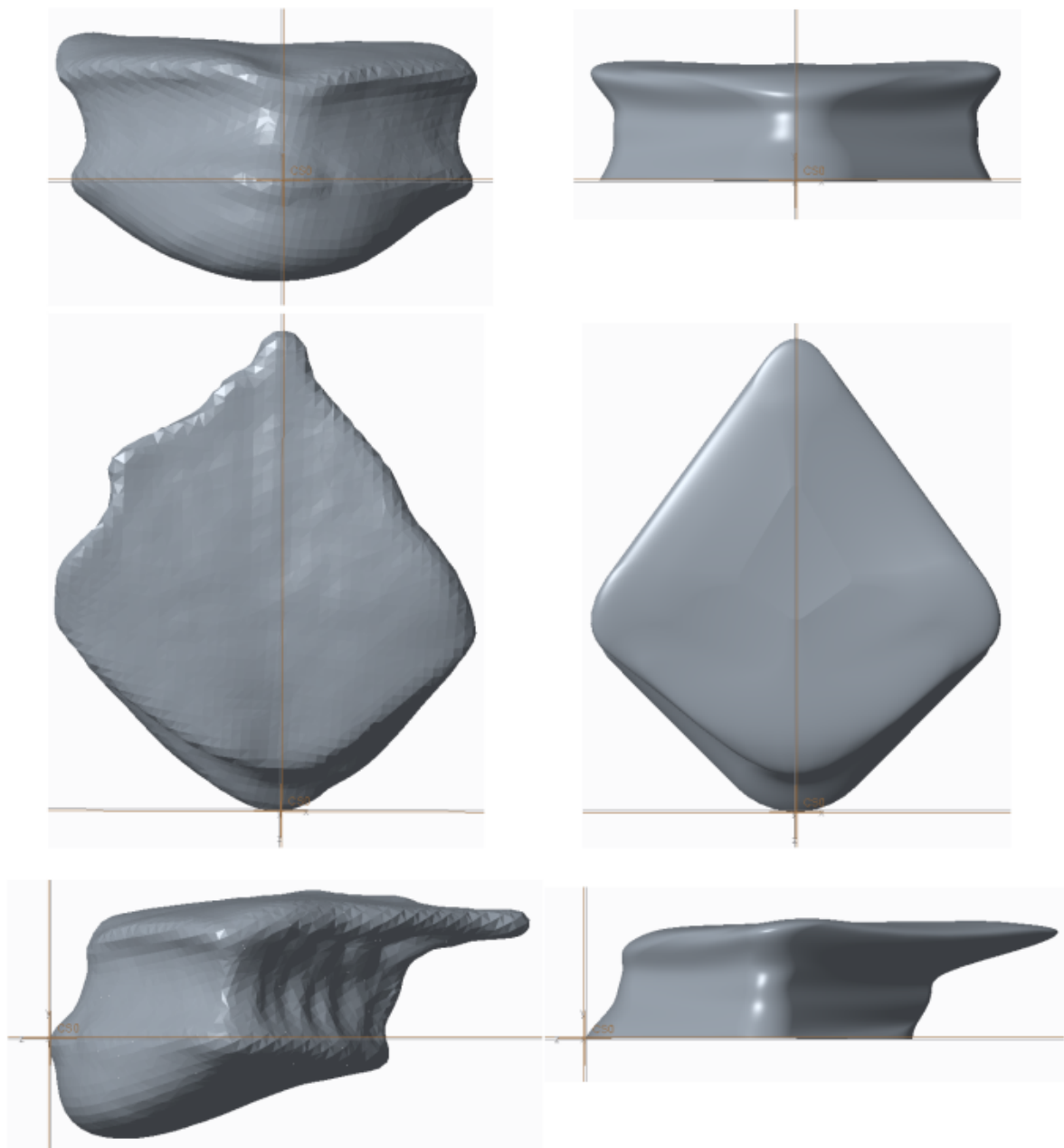


Figure 24: Comparison of sampled scale (left) and simplified scale (right).

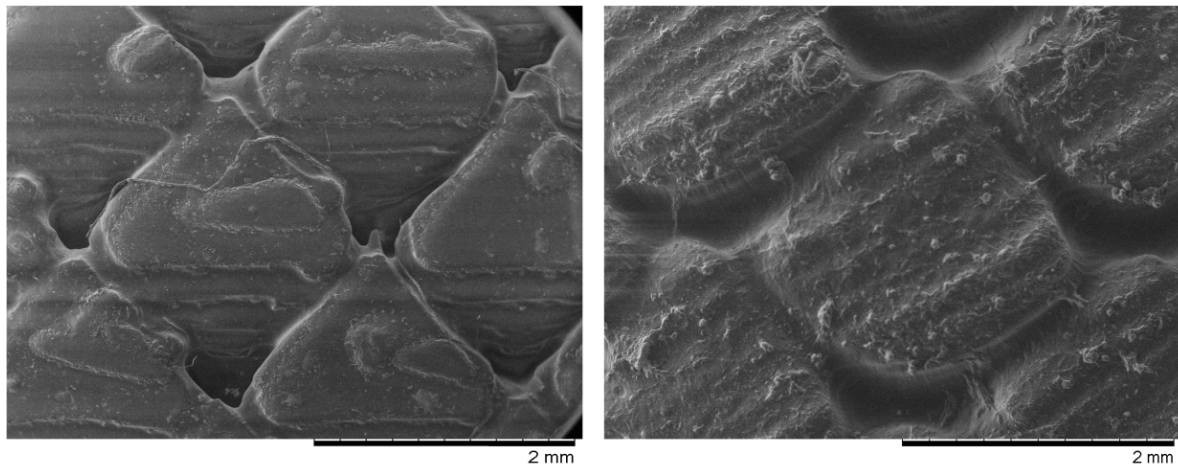


Figure 25: SEM image of printed scale from the university of Leeds (left), and a commercial company (right).

seem to have been merged together during the printing process. Further tests are being carried out at the University of Nottingham, who have access to printers of a much higher resolution than those used to generate the samples of Figure 25.

7 Application of Reynolds-Averaged Navier-Stokes to a Periodic Shark Scale Domain

This section details the mesh independence study of the flow over a periodic array of scales using a RANS turbulence closure. Section 2 indicated a large gap in the literature concerning the effect of shark scale geometry on a flow. RANS methods have the potential to investigate this without large expense, but require validation. When available, the results of the present study will be validated against LES data.

7.1 Mathematical Model

The present work adopts a steady state RANS turbulence closure using OpenFOAM; an open source finite volume code. The fundamental equations are the Reynolds averaged equations, first introduced in Section 2, and the continuity equation. These are defined as

$$\langle U_j \rangle \frac{\partial \langle U_i \rangle}{\partial x_j} = - \frac{\partial \langle P \rangle}{\partial x_j} + \nu \left(\frac{\partial \langle U_j \rangle}{\partial x_i} + \frac{\partial \langle U_i \rangle}{\partial x_j} \right) + \frac{\partial \langle u_i u_j \rangle}{\partial x_j}, \quad (18)$$

and,

$$\frac{\partial \langle U_i \rangle}{\partial x_i} = 0, \quad (19)$$

where $\langle \rangle$ represents the ensemble average. This particular work adopts the $k - \omega$ Shear Stress Transport (SST) model, first proposed by Menter (1994). This closure estimates the Reynolds stresses by solving a transport equation for the turbulent kinetic energy, k , and the turbulent frequency, ω . The standard $k - \omega$ model is known for its ability to resolve boundary layer flows more accurately than other two-equation alternatives, such as $k - \epsilon$. These quantities are related by $\epsilon = \omega k$. However, it has failed to replace the $k - \epsilon$ model as the industry standard due to its poor performance in freestream flows (Menter et al., 2003). This issue is accounted for in the $k - \omega$ SST model by adding an additional term to the ω equation. The result is essentially a blending between the near wall $k - \omega$ model, and the freestream $k - \epsilon$ model. There are many other turbulence closures that could be appropriate for this problem. The two equation $k - \omega$ SST model was chosen as a compromise between the more accurate, but computationally expensive, Reynolds Stress Transport equations, and the less accurate, but cheaper, one-equation models. The solution dependency on turbulence closure will be investigated after obtaining a mesh independent solution.

The $k - \omega$ SST model adopts the turbulent viscosity hypothesis, whereby the Reynolds stresses are estimated by,

$$\langle u_i u_j \rangle = \frac{2}{3} k \delta_{ij} - \nu_T \left(\frac{\partial \langle U_i \rangle}{\partial x_j} + \frac{\partial \langle U_j \rangle}{\partial x_i} \right), \quad (20)$$

where ν_T is the turbulent viscosity. The turbulent viscosity is assumed to be related to k and ω by,

$$\nu_T = \frac{a_1 k}{\max(a_1 \omega, F_1 \sqrt{2S_{ij} S_{ij}})}, \quad (21)$$

where a_1 is an empirical constant, F_1 is a blending function, and S_{ij} is the rate of strain tensor,

$$S_{ij} = \frac{1}{2} \left(\frac{\partial \langle U_i \rangle}{\partial x_j} + \frac{\partial \langle U_j \rangle}{\partial x_i} \right). \quad (22)$$

The blending function is a hyperbolic tangent function, such that it takes the value 0 near the wall and 1 far from the wall. The transport equation for k is defined as,

$$\frac{\partial(\langle U_j \rangle k)}{\partial x_j} = \mathcal{P} - \beta^* \omega k + \frac{\partial}{\partial x_j} \left[(\nu + \sigma_k \nu_T) \frac{\partial k}{\partial x_j} \right], \quad (23)$$

where β^* and σ_K are empirical constants, and \mathcal{P} is the production of turbulent kinetic energy,

$$\mathcal{P} = -\langle u_i u_j \rangle \frac{\partial \langle U_i \rangle}{\partial x_j}. \quad (24)$$

(24) is solved by using the definition of $\langle u_i u_j \rangle$ in (21). The equation for ω is given by,

$$\frac{\partial(\langle U_j \rangle \omega)}{\partial x_j} = \frac{\alpha}{\mu_T} \mathcal{P} - \beta \omega^2 + \frac{\partial}{\partial x_j} \left[(\nu + \sigma_\omega \nu_T) \frac{\partial \omega}{\partial x_j} \right] + 2(1 - F_2) \frac{\sigma_d}{\omega} \frac{\partial k}{\partial x_j} \frac{\partial \omega}{\partial x_j}, \quad (25)$$

where α , β , σ_ω , and σ_d , are empirical constants, $\mu_T = \rho \nu_T$, and F_2 is a blending function of the same form as F_1 . The choices of F_1 , F_2 , and the empirical constants, are detailed by Menter (1994). They are essentially chosen to fit the model to a range of flow problems. The blending functions are unique to the SST version of $k-\omega$; they control the blending process between the near wall $k-\omega$ model and the freestream $k-\epsilon$. The three component momentum equation, (18), continuity equation, (19), transport of kinetic energy equation, (23), and the transport of turbulent frequency equation, (25), are our closed system of equations.

7.2 Numerical Implementation

The system of equations, defined in Section 7.1, are discretised using finite volume methods. Gradient and Laplacian terms are discretised using standard Gaussian integration. Linear interpolation is adopted in order to calculate face fluxes from the variables stored at cell centres. In order to ensure stability, the interpolation scheme of the convective terms is a mixture of upwind and linear methods, whereby in regions of rapidly changing gradient an upwind scheme is adopted (but still accurate to second order). The SIMPLE algorithm of Caretto et al. (1973) is adopted in order to couple the continuity and momentum equations (see Appendix A for details). Linear algebra is solved using

Gauss-Seidel algorithms for all equations apart from pressure, which adopts a generalised multigrid method. Convergence is assessed by monitoring the pressure, velocity, and turbulence scalars, at several locations near the surface of the scales. The residual errors from the linear algebra is also monitored.

The finite volume mesh is constructed from the domain observed in Figure 26. The CAD model, defined in Section 6, is arranged in a staggered array, the dimensions of which can be observed in Figure 27, where H_s is the height of the scale. The three points, x_1 , x_2 , and x_3 , are used to define wall-normal profiles by which mesh independence is assessed. Since the fields solved by the RANS formulation are ensemble averaged, we can assume that the flow over each scale is identical. We therefore define periodic boundary conditions in the streamwise (x) direction, and symmetry boundaries in the z direction. The shark scale scale surface is placed at the base of the channel, $y = 0$, and a flat wall is placed at $y = 2\delta$, where δ is the half-channel height. The bulk flow Reynolds number is set to $Re_b = \delta U_b / \nu = 13500$, where U_b is the bulk velocity. For a smooth walled channel, this corresponds to a shear Reynolds number of $Re_\tau = 395$. The wall-unit length scale is therefore $\delta_\nu = \nu / u_\tau = 1/395$ which is used to estimate the cell sizes when constructing the meshes observed in Figure 26.

SnappyHexMesh software is used to mesh the domain. Refinement is based on a cell level specification, whereby each level splits the cell size of the previous level into 8 smaller cells. Level 0 corresponds to the base mesh size, and a level 1 cell would have each of the level 0 cells edges halved in length. The effect of this can be observed in Figure 28. As the distance from the scales increases, there are several jumps in cell size before reaching that of the base mesh. The location of these jumps, the size of the base mesh, and the maximum level size, are varied between each mesh case.

Three cases are presented in this work, each with a mesh of increasing resolution. By using estimated wall-unit length scale of $\delta_\nu = 1/395$, the mesh is created in wall

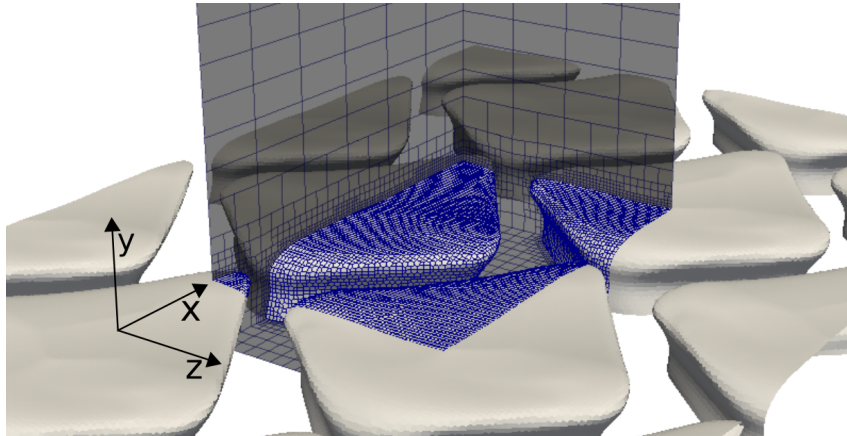


Figure 26: 3D periodic domain for the RANS simulations. Streamwise direction is positive in x .

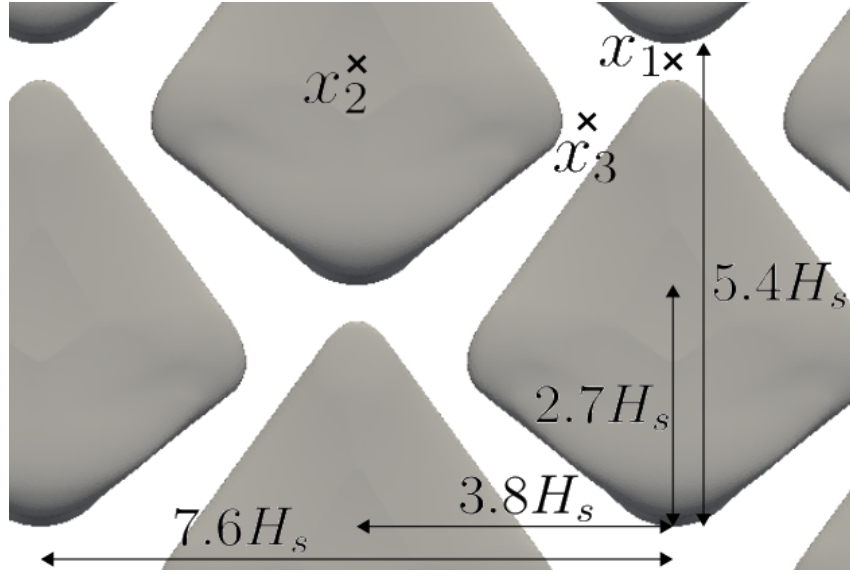


Figure 27: Staggered denticle array, with dimensions normalised by the denticle height. x_1 , x_2 , and x_3 , are the locations at which profiles of variables are taken in Section 7.3.

units. The scale height is set to $H_s^+ = 20$, which will be varied in future experiments. Using the periodic dimensions specified in Figure 27, this corresponds to a domain size of $5.4H_s \times 2\delta \times 7.6H_s = 108 \times 790 \times 152$ in wall units. The three meshes can be observed in Figure 28, and the statistics of each case are presented in Table 6. At least 90 % of the cells in the domain lie below $y^+ < 40$ for each of the cases. case C1 is the ‘coarse’ solution, with a maximum cell size of 18, and large jumps between cell sizes. C2 has finer cells but still has large jumps. C3 is the same specifications as C2 but has smoother transitions i.e more cells in each layer. The size of the cells covering the STL shark scale are very similar for C2 and C3 cases.

Mesh independence is assessed in two ways; the y dependence of several variables is plotted at three locations, specified in Figure 27. In addition to this, the errors associated with pressure and absolute velocity gradient, over the shark scale surface, are analysed. The error associated with a scalar ϕ is assessed by interpolating the solution over the scale surface onto the finest scale surface (C3). This ensures that cells coincide, and solutions

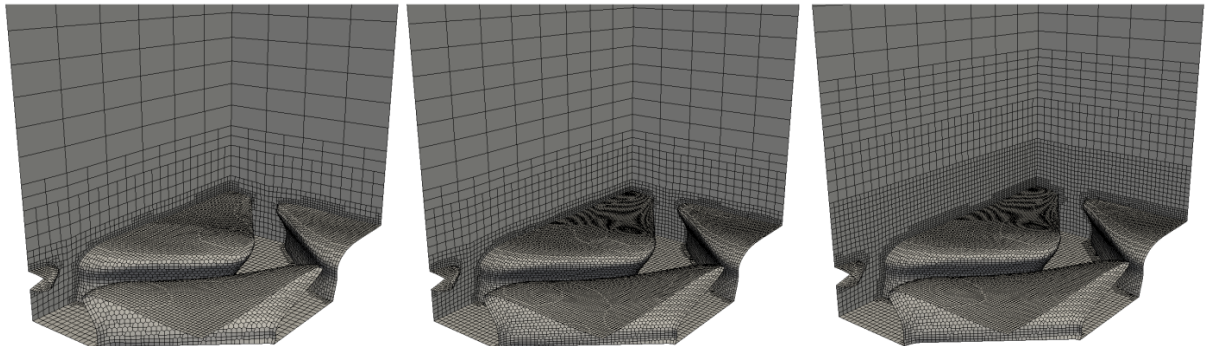


Figure 28: Three meshes corresponding to C1 (left), C2 (center), and C3 (right).

Table 6: Mesh statistics.

Case	Max. cell size Δy_{max}^+	Total cell count N_t	Cell count near scales $N(y^+ < 40)$	Number of faces on the scales N_s
C1	18	39396	37572	7296
C2	14	75417	71617	12571
C3	14	117065	113105	12167

can be directly compared. The values of ϕ over the finest mesh are denoted ϕ_{REF} , and are scaled such that their minimum value is 0 and their maximum is 1:

$$\bar{\phi}_{REF} = \frac{\phi_{REF} - \min(\phi_{REF})}{\max(\phi_{REF}) - \min(\phi_{REF})}. \quad (26)$$

where $\bar{\phi}_{REF}$ is the scaled reference value of ϕ . Similarly, ϕ , the coarse mesh solution, is translated to a minimum value of 0 and then scaled by the same amount as ϕ_{REF} :

$$\bar{\phi} = \frac{\phi - \min(\phi)}{\max(\phi_{REF}) - \min(\phi_{REF})}. \quad (27)$$

The error is defined as the root-mean-square of the difference between ϕ and ϕ_{REF} :

$$\text{Error}(\phi) = \sqrt{(\bar{\phi}_{REF} - \bar{\phi})^2} \quad (28)$$

7.3 Results and Discussion

The purpose of this section is to determine whether the current cases are mesh independent; for this reason, comparisons between smooth and sharkskin surfaces are not discussed. These comparisons will be made when LES data sets are available for validation.

Figures 29 to 35 indicate very little difference between the profiles of velocity, turbulent kinetic energy, and turbulent frequency, for the three cases. Discrepancies can be

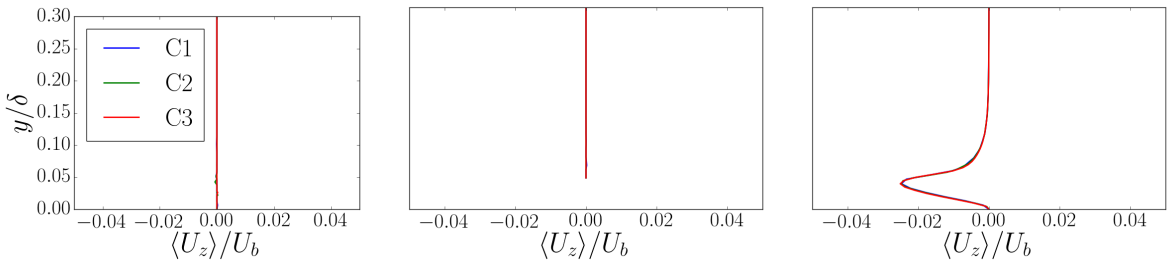


Figure 29: Profiles of cross-stream velocity, normalised by the bulk velocity. Locations of the profiles are x_1 (left), x_2 (center), and x_3 (right), which can be observed in Figure 27.

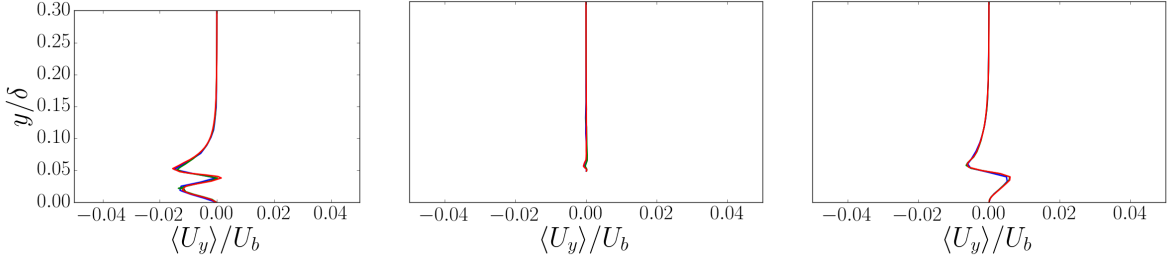


Figure 30: Profiles of wall-normal velocity, normalised by the bulk velocity. Locations of the profiles are x_1 (left), x_2 (center), and x_3 (right), which can be observed in Figure 27. For legend, see Figure 29.

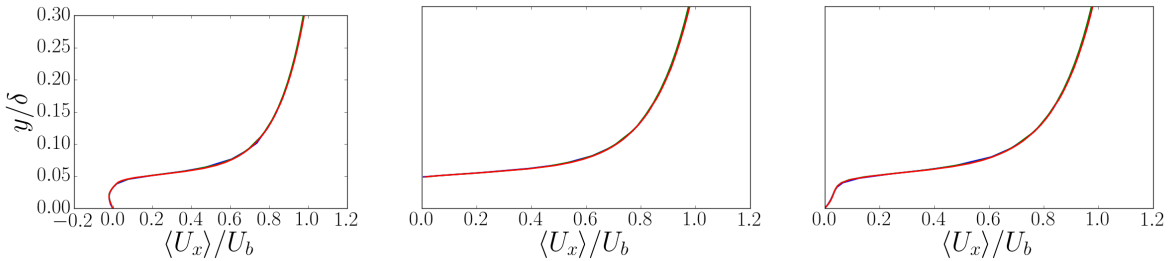


Figure 31: Profiles of streamwise velocity, normalised by the bulk velocity. Locations of the profiles are x_1 (left), x_2 (center), and x_3 (right), which can be observed in Figure 27. For legend, see Figure 29.

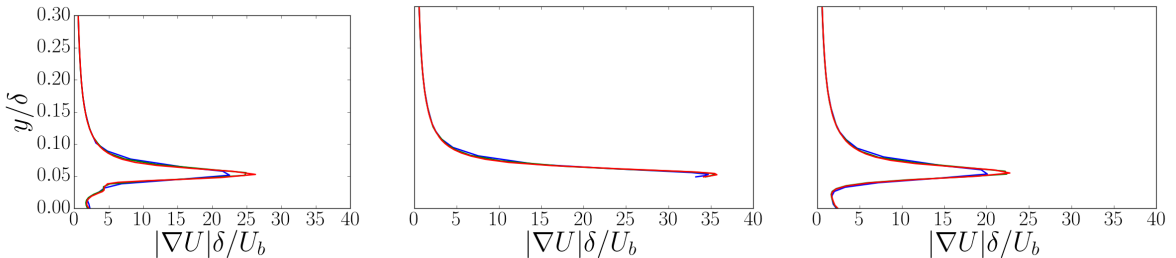


Figure 32: Profiles of absolute velocity gradient, normalised by the bulk velocity and half channel height. Locations of the profiles are x_1 (left), x_2 (center), and x_3 (right), which can be observed in Figure 27. For legend, see Figure 29.

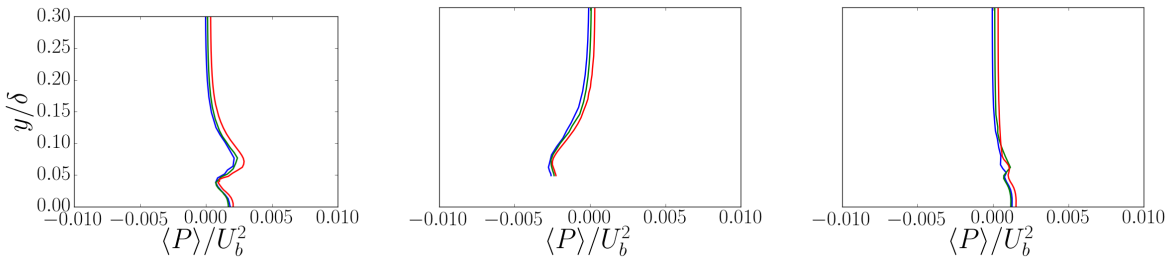


Figure 33: Profiles of pressure, normalised by the square of the bulk velocity. Locations of the profiles are x_1 (left), x_2 (center), and x_3 (right), which can be observed in Figure 27. For legend, see Figure 29.

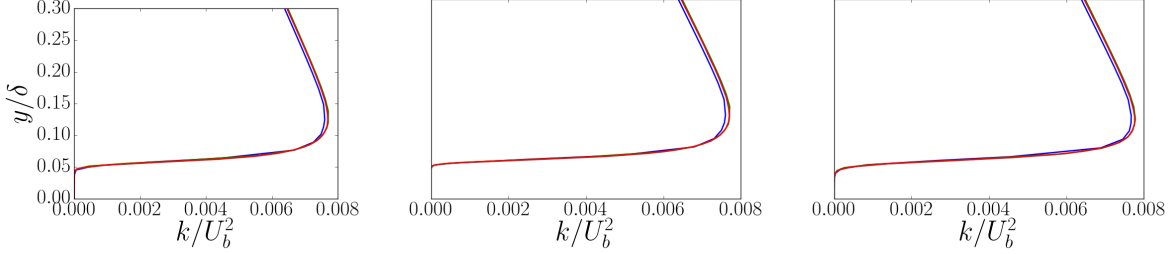


Figure 34: Profiles of turbulent kinetic energy, normalised by the square of the bulk velocity. Locations of the profiles are x_1 (left), x_2 (center), and x_3 (right), which can be observed in Figure 27. For legend, see Figure 29.

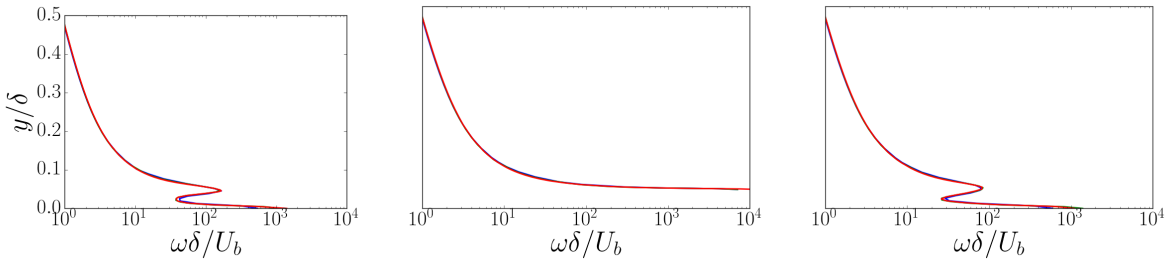


Figure 35: Profiles of turbulent frequency, normalised by the bulk velocity and half channel height. Locations of the profiles are x_1 (left), x_2 (center), and x_3 (right), which can be observed in Figure 27. For legend, see Figure 29.

observed between C1 and the other two cases when considering the magnitude of velocity gradient profiles; the maximum point is under predicted for the x_1 and x_3 profiles. It is only when considering the profiles of pressure that the C2 profile becomes separate from the C3 profile. A possible reason for this is that the pressure is not explicitly stated by the adopted boundary conditions; the walls and symmetry planes adopt Neumann conditions, and the periodic boundaries specify an iterative pressure gradient which maintains a constant mass flux. For this reason, only the pressure gradient is specified at the boundaries. To overcome this, a reference pressure of 0 is assigned to a fixed location on the top wall. Since the mesh density varies between the different cases, the interpolation between this point and the near wall cells could be the cause of the differences observed in Figure 33. This is certainly something to investigate in the future.

Figures 36 and 37 show how the errors associated with velocity gradient and pressure vary over the surface of the scale. The errors are calculated using (26) to (28), where the reference case is C3. It should be noted that the swirling and feint checker-board patterns are likely features of the interpolation, but the figures do highlight the regions of the largest error. When considering the pressure, the error is negligible for both cases over most of the scale surface. However, errors exceed 10 % near the leading edge of the C1 case, and 5 % for the C2 case. These are further emphasised when considering the velocity gradient; the high error regions for pressure and velocity gradient coincide for

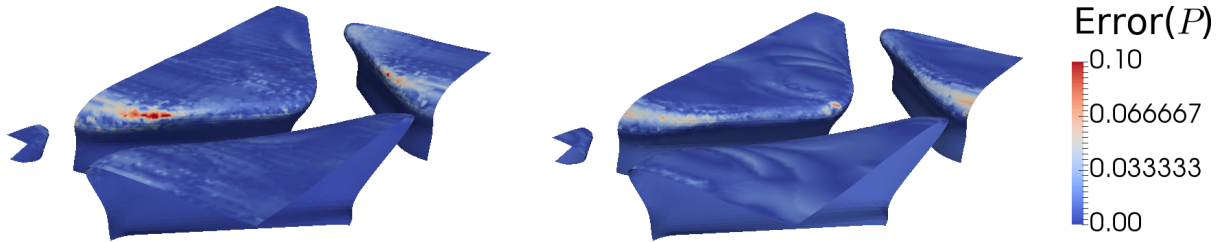


Figure 36: Contours of the error, associated with pressure, between C1 and C3 (left), and C2 and C3 (right), over the scale surface.

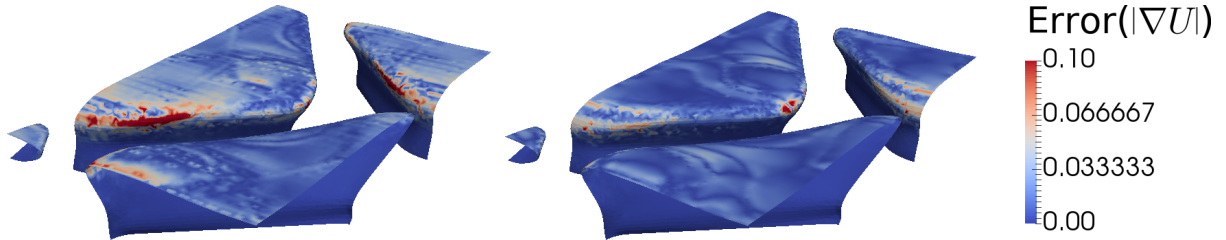


Figure 37: Contours of the error, associated with velocity gradient, between C1 and C3 (left), and C2 and C3 (right), over the scale surface.

the C1 case, but cover a larger proportion of the scale for the velocity gradient. The location of maximum velocity gradient error for the C2 case is located on the side edge of the scale, covering only a few cells. However, the number of cells covering the scale surface is nearly identical for the C2 and C3 cases (see Table 6). This suggests that the smoother transition between the fine surface mesh and the background mesh has larger implications on the near-surface flow than the fields captured by the profile plots.

When comparing the profile plots and the error contours several conclusions can be drawn; the background mesh captures the flow field well for all three cases, although discrepancies do appear when considering the profiles of pressure. These will be investigated in future work. In addition to this, the profiles indicate little dependence on the resolution of the scale surface mesh. However, the surface mesh does have large implications on the flow close to the scales. In addition to this, smooth transitions from the fine surface cells to the background mesh have a large effect on the near-surface flow. Further work will investigate methods of applying the smooth transitions in order to maintain mesh independence but reduce the total number of cells. The current models are not expensive to run, but when extending these mesh parameters to an LES, the additional cells will become significant.

8 Large Eddy Simulation (LES) of a Channel Flow

LES is adopted in this project in order to investigate the effects of sharkskin on the turbulent structures in a boundary layer. The results will also be used to validate the RANS study of Section 7. This study will be carried by simulation a fully developed channel flow, with and without shark scales attached to one wall. The present work carries out LES on a smooth walled channel, in order to validate the numerical methods, the turbulence closure, and provide a reference case for comparisons in future work. This is carried out at a Reynolds number of $Re_\tau = 180$, allowing the DNS database of Vreman and Kuerten (2014) to be used for validation.

8.1 Mathematical Model

The equations solved in the present work are detailed in this section, although a full derivation can be found in Appendix B. Two models are adopted, the Smagorinsky (1963) model and the dynamic Lagrangian model of Meneveau et al. (1996). Both of these models solve filtered continuity and momentum equations:

$$\frac{\partial \bar{U}_i}{\partial x_i} = 0, \quad (29)$$

and

$$\frac{\partial \bar{U}_i}{\partial t} + \frac{\partial \bar{U}_i \bar{U}_j}{\partial x_j} + \frac{\partial \tau_{ij}^r}{\partial x_j} - \frac{\partial \bar{\sigma}_{ij}}{\partial x_j} = -\frac{\partial \bar{P}}{\partial x_i}, \quad (30)$$

where the filtered velocity and pressure fields are given by $\bar{U}_i = U_i - u'_i$ and $\bar{P} = P_i - p'_i$, where u'_i and p'_i are the residual fields. τ_{ij}^r represents the anisotropic residual stress term, and accounts for the effect of sub-grid scale motion on the filtered fields:

$$\tau_{ij}^R \equiv \tau_{ij}^r + \frac{1}{3} \tau_{kk}^R \delta_{ij} \equiv \bar{U}_i \bar{U}_j - \bar{U}_i \bar{U}_j, \quad (31)$$

where τ_{ij}^R represents the residual stress tensor; its isotropic component is incorporated into the residual pressure term in (30). The model of Smagorinsky (1963) relates this stress term to a turbulent viscosity:

$$\tau_{ij}^r = -2(C_s \bar{\Delta})^2 |\bar{S}| \bar{S}_{ij}, \quad (32)$$

where c_s is the Smagorinsky constant, $\bar{\Delta}$ is the filter width (taken as the cube root of the local cell volume), and \bar{S} and \bar{S}_{ij} are given by,

$$\bar{S}_{ij} = \frac{1}{2} \left(\frac{\partial \bar{U}_i}{\partial x_j} + \frac{\partial \bar{U}_j}{\partial x_i} \right), \quad |\bar{S}| = (2 \bar{S}_{ij} \bar{S}_{ij})^{1/2}. \quad (33)$$

The present work adopts a Smagorinsky constant of $C_s = 0.17$. Thus, the Smagorinsky model estimates τ_{ij}^r using an algebraic relationship with the fluid rate of strain, which is subsequently used to close the momentum and continuity equations, (30) and (29). The dynamic Lagrangian model of Meneveau et al. (1996) addresses the limitation that C_s does not vary in space or time. By applying a second filter to the momentum equation, a relationship for C_s can be derived by taking the difference between the once- and twice-filtered velocity fields;

$$C_s^2 = \frac{(L_{ij}M_{ij})_{ave}}{(L_{ij}M_{ij})_{ave}} = \frac{f_{LM}}{f_{MM}}, \quad (34)$$

where L_{ij} and M_{ij} can be calculated from the filtered velocity field:

$$L_{ij} = \widetilde{\overline{U}_i \overline{U}_j} - \widetilde{\overline{U}_i} \widetilde{\overline{U}}_j, \quad (35)$$

and,

$$M_{ij} = 2\overline{\Delta}^2 \widetilde{|S|} \widetilde{S}_{ij} - 2\widetilde{\overline{\Delta}}^2 |\widetilde{S}| \widetilde{S}_{ij}, \quad (36)$$

where the tilde represents the second filtering operator, and $\widetilde{\overline{\Delta}} = 2\overline{\Delta}$ is the respective filter width. Meneveau et al. (1996) construct relaxation equations for f_{LM} and f_{MM} , equivalent to averaging along particle paths with a relative weight $\exp[-(t-t')/T]$, where t' is the earlier time and T is the relaxation time:

$$\frac{\partial f_{LM}}{\partial t} + \frac{\partial}{\partial x_j} (\overline{U}_j f_{LM}) = \frac{1}{T} (L_{ij} M_{ij} - f_{LM}), \quad (37)$$

$$\frac{\partial f_{MM}}{\partial t} + \frac{\partial}{\partial x_j} (\overline{U}_j f_{MM}) = \frac{1}{T} (M_{ij} M_{ij} - f_{MM}). \quad (38)$$

The present work adopts a relaxation time of $T = 1.5\overline{\Delta}(f_{LM}f_{MM})^{-1/8}$, as recommended by Meneveau et al. (1996). Subsequently, the memory time is reduced in regions of high straining (high f_{MM}) and large nonlinear energy transfer (high f_{LM}). Although much less susceptible to negative values (Meneveau et al., 1996), f_{LM} is clipped in order to ensure physicality (positive C_s^2). The filtered momentum and continuity equations are therefore solved by the following steps: M_{ij} and L_{ij} are calculated from the filtered fields using (35) and (36); a top-hat filter is adopted for the second filtering operator. We then solve the relaxation equations, (61) and (62) and calculate the Smagorinsky coefficient from (34). This is then used to calculate the residual stress, as per the standard Smagorinsky model. A more detailed derivation of the filtered equations can be found in Appendix B.

8.2 Numerical Implementation

The equations are solved using OpenFOAM, a finite volume platform. They are discretised over a channel of dimensions $12.6\delta \times 2\delta \times 4.2\delta$ where δ is the channel half height.

Similar dimensions are used by several authors such as Moser et al. (1999), and Vreman and Kuerten (2014) for a Reynolds number of $Re_\tau = 180$, although the influence of domain size on the turbulent statistics is still poorly understood (Vreman and Kuerten, 2014). Two simulations are presented in this report; one adopting the Smagorinsky (1963) closure and one adopting the dynamic Lagrangian closure of Meneveau et al. (1996).

The mesh statistics are presented in Table 7. The total number of cells is $\sim 4M$, much fewer than an equivalent finite difference DNS of Vreman and Kuerten (2014) who used $\sim 33M$ grid points. The mesh is uniform in x and z , but cells are clustered near the walls in the y direction in order to capture the large gradients in pressure and velocity near the wall. Periodic boundary conditions are applied in both streamwise and spanwise direction with a forcing term added to the momentum equation (30) in order to maintain a constant bulk Reynolds number in the x direction. The forcing term is derived by decomposing the pressure gradient into an average and fluctuating component; the average pressure gradient is adjusted each timestep in order to ensure a fixed mean velocity through the periodic faces, $\bar{\mathbf{U}}_{ave}$. A description of this technique is presented by Murthy and Mathur (1997). A convenient choice for the parameters ν and $\bar{\mathbf{U}}_{ave}$ fix the bulk Reynolds number to $Re_b = 2800$, corresponding to a shear Reynolds number of $Re_\tau \approx 180$. The choice of fixing the bulk flow Reynolds number is more natural when considering the validation of results against experiments later this year. For a channel flow, Re_τ can be determined from the pressure gradient over the periodic boundary by applying a force balance over the domain:

$$u_\tau^2 = \frac{\tau_w}{\rho} = \delta \frac{\partial P}{\partial z} \Big|_{ave}. \quad (39)$$

A convenient choice of parameters are $\delta = 1$ and $\nu = 1/180$ resulting in an average shear velocity of $u_\tau \approx 1$ and $Re_\tau \approx 180$. The initial state makes use of a perturbation utility in OpenFOAM which adds instabilities to a flow profile of mean velocity $\bar{\mathbf{U}}_{ave}$. These instabilities grow between timesteps until a statistically steady and turbulent state is present.

The momentum (30), continuity (29), and the two Lagrangian transport equations (37) and (38) are discretised using second order schemes in both space and time. Backward Euler is adopted for discretisation in time and Gaussian integration in space. Linear interpolation is adopted in order to interpolate values from cell centres to cell faces. The PISO algorithm (Pressure-Implicit with Splitting of Operators) of Issa (1986) is adopted in order to solve the continuity and momentum equations (see Appendix A for details). The subsequent Laplacian equation for pressure is solved using a generalised multigrid

Table 7: Mesh statistics for the two LES cases.

N_x	N_y	N_z	Δx^+	Δz^+	Δy_{min}^+	Δy_{max}^+
160	128	192	4.7	11.8	0.18	4.5

method. An adaptive time-stepping scheme is adopted in order to ensure the Courant number does not exceed 0.5. Statistical averaging is carried out between the time intervals $t = 10\delta/u_\tau$ and $t = 40\delta/u_\tau$. This interval is much smaller than those adopted by Kim et al. (1987) and Vreman and Kuerten (2014), the impact of which will be discussed in Section 8.3.

Post-processing is carried out in MATLAB; Statistical quantities, such as means and standard deviations, are looped through each time-step directory and averaged in x and z . The results of which are compared to those of a spectral DNS code of Vreman and Kuerten (2014).

8.3 Results and Discussion

The calculated Reynolds numbers for the two simulations are compared against the DNS code in Table 8. Both simulations compute a slightly lower Reynolds number than the DNS, due to the method of calculating the forcing term. The target bulk Reynolds number was 2800, thus these small discrepancies are expected. The coefficient of friction agrees well with the DNS for the Smagorinsky model, but is under predicted by 1.11% by the dynamic Lagrangian model. This will be further discussed when investigating variable profiles.

Little discrepancy can be observed from the velocity profiles of Figure 38. Small differences can be observed in regions of high velocity gradient for the Smagorinsky model. Much larger discrepancies are present in the root-mean-square (rms) statistics. Figure 39 indicates that the Smagorinsky models underpredicts the maximum values significantly in both the wall-normal and cross-stream directions. The near-wall gradients are also poorly captured by the Smagorinsky model, suggesting that the model perform poorly in these regions. The dynamic-Lagrangian model performs well, almost matching the DNS in all three directions. The small discrepancy in magnitude can be accounted for by the turbulent kinetic energy captured by the sub-grid scale stress term. THE RMS of velocity profiles collapse for both models at $y = \delta$, suggesting that the dynamic Lagrangian model has little impact in regions far from the wall. The Reynolds stresses are well predicted by the dynamic model but the maximum is under-predicted by the Smagorinsky model.

Table 8: Comparison of global statistics between two LES cases and a DNS.

	Re_b	% to DNS	Re_τ	% to DNS	Re_c	% to DNS	C_f	% to DNS
DNS (Vreman and Kuerten, 2014)	2825	-	180	-	3290	-	0.00812	-
Smagorinsky model	2802	-0.81	178.5	-0.83	3269	-0.64	0.00817	0.62
dynamic Lagrangian model	2800	-0.88	177.4	-1.44	3266	-0.73	0.00803	-1.11

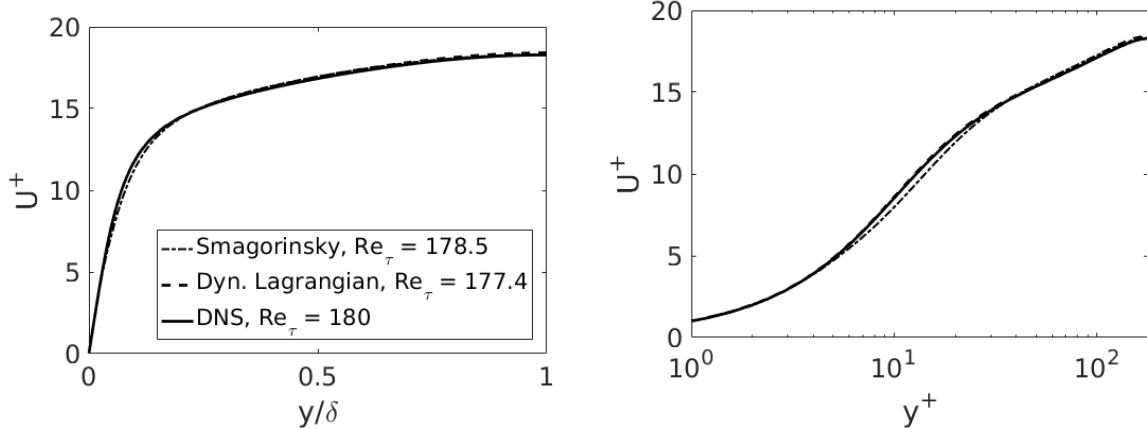


Figure 38: Comparison of mean velocity profiles for two LES cases and the DNS of Vreman and Kuerten (2014).

A reasonable explanation for this is expressed by Pope (2001), who suggests that, for low Reynolds number flows, the fixed constant C_s must be reduced in order to predict the sub-grid scale stresses. Since the Reynolds number is low, this explanation seems reasonable.

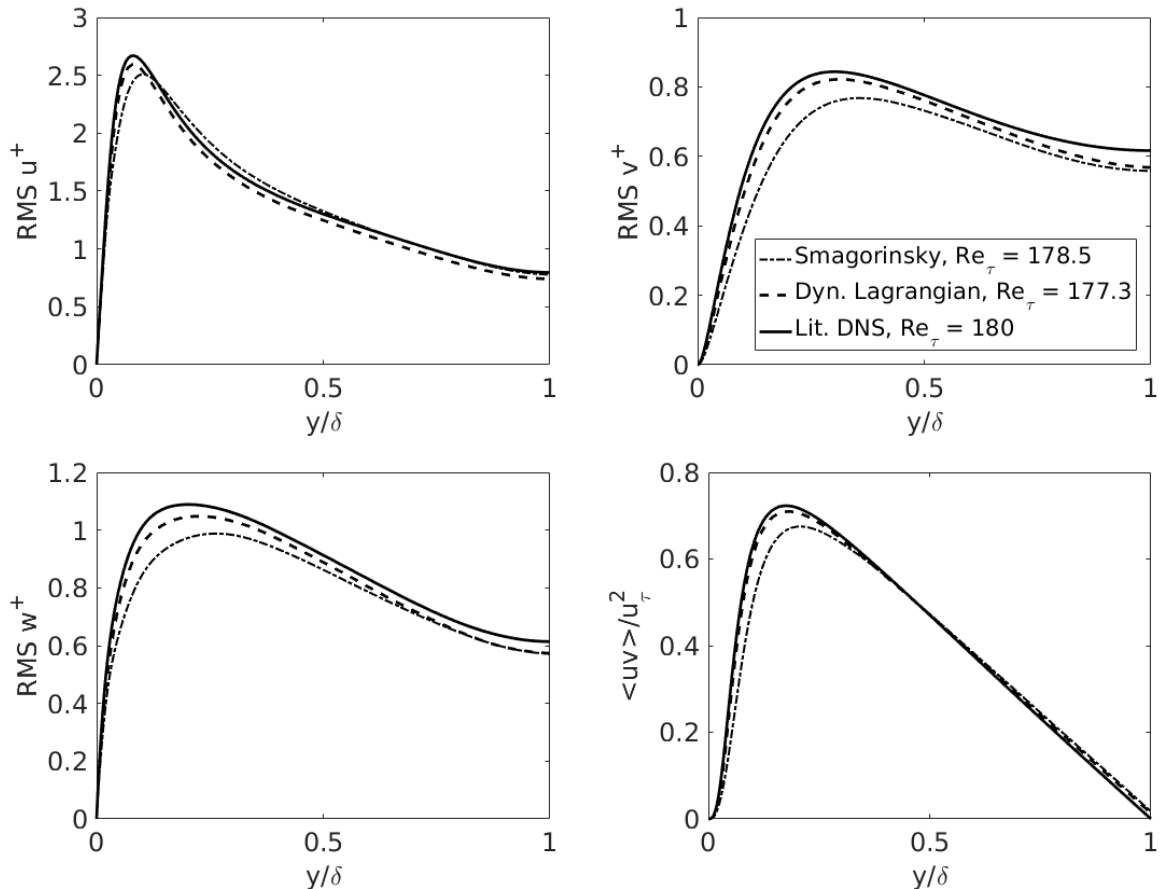


Figure 39: Comparison of root-mean-square velocity profiles, and the Reynolds stresses, for two LES cases and the DNS of Vreman and Kuerten (2014).

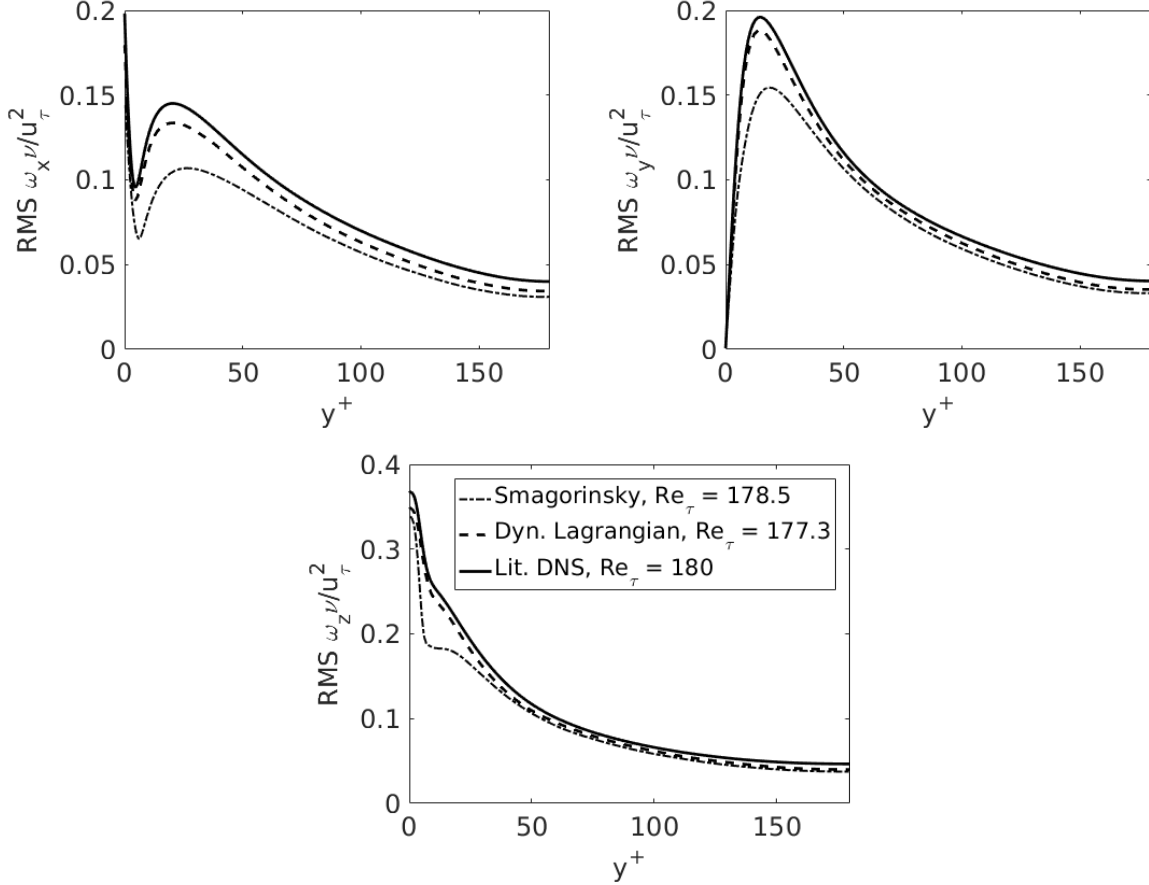


Figure 40: Comparison of RMS Vorticity for two LES cases and the DNS of Vreman and Kuerten (2014).

The rms of vorticity profiles (Figure 40) similarly indicate that the dynamic model predicts the flow much better close to the wall. The Smagorinsky model significantly underpredicts the vorticity fluctuations below $y^+ \approx 50$. Near the centre of the channel there is little difference between the two simulations. Again, this suggests that the dynamic model is most effective near the wall.

8.4 Conclusions and Further Work

Two LES models have been assessed by their ability to predict a fully developed channel flow, validated against a DNS dataset (Vreman and Kuerten, 2014). Both the Smagorinsky model (Smagorinsky, 1963) and the dynamic Lagrangian model (Meneveau et al., 1996) predict the velocity profiles well. Deviations are more substantial when investigating the RMS velocity, RMS vorticity, and Reynolds stresses. The Smagorinsky model generally underpredicts the magnitude of the fluctuations for all three components of vorticity, and the cross-stream and wall-normal fluctuations of velocity. The dynamic Lagrangian model compares well against the DNS for these statistics, accurately capturing the features close to the wall. However, the statistical dependence on the temporal

averaging window has not yet been investigated. In addition to this, the effect of using level-based mesh refinement (described in Section 7) must be validated before simulating the flow over an array of shark scales. Once the Reynolds number of the shark scale simulations has been determined, these two dependencies will be investigated.

9 6 Month Plan

The Gantt chart of Figure 41 indicates several different work packages, some of which are dependent on the completion of others. The experimental work is the main priority over the coming months since these results will form the first publication. The main risk associated with this work package is the 3D printing of the denticle arrays. There is potential to work in collaboration with the University of Nottingham who are currently printing samples of these scales. If the desired resolution can be met, then the arrays will be printed and the LDA experiments can commence.

The LES work package is also partly reliant on the 3D printing capabilities. The estimates of the scale size will be necessary if experiments are to match those of the numerics. However, there are other work packages that can be completed while the printing experiments are taking place. The experimental set up is also dependent on further CAD developments; since a full 500 mm by 100 mm array is unlikely to be printed in one section, the CAD model will have to be split. Care must be made in order to ensure the joints do not interfere with the surface. In addition to this, a new experimental plan must be developed in order to account for different grid sizes and sampling times.

RANS dependency studies also need further investigation, such as the dependencies on the turbulence closures, the number of scales in the periodic domain, and the discretisation schemes. The LES study is loosely dependent on the RANS studies since they provide an estimate to the required grid size.

10 High Level Plan

The main objectives of Section 4 are given the following timescales:

- Complete and write up LDA results for the flat plate flow over both smooth and two 3D printed shark scale surface (by Dec 2017).
- Carry out a LES for the same shark scales at a feasible scale width (to be defined by the RANS studies in Summer 2017), and compare findings against a flat plate LES, and a RANS model (by Mar 2018).
- If RANS methods can be validated then carry out a parametric analysis on the effect of shark scale geometry on the fluid flow (by July 2018).

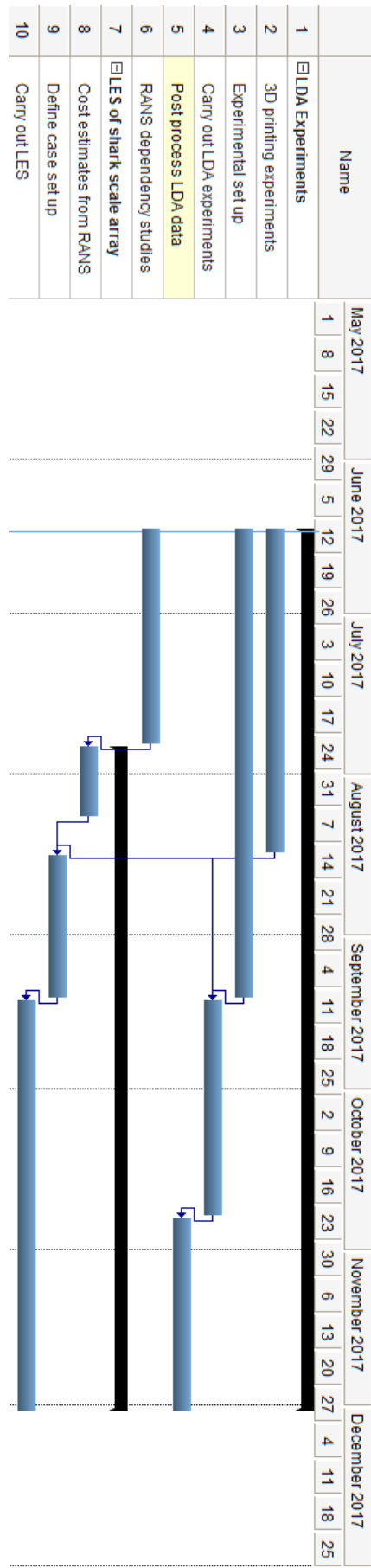


Figure 41: Gantt chart for the months June 2017 - Dec 2017.

- Carry out PIV and LES/RANS (depending on the validation of the models) for a separating flow, with and without scales (by March 2019).

11 Publications, Conferences, and Placements

Four potential papers could be published if the above work packages can be completed:

1. An experimental investigation into the effects of smooth and ribletted sharkskin denticles on a flat plate boundary layer, using Laser Doppler Anemometry.
2. Large eddy simulation of smooth and ribletted sharkskin denticles in a turbulent channel flow.
3. A parametric study of the effects of sharkskin denticle geometry on a turbulent channel flow, using numerical methods.
4. An experimental investigation into the effects of sharkskin denticles on separating flows, using Particle Image Velocimetry.

There is potential for a placement with another UK university in order to carry out experiments on the flat plates with force balances. These results would complement the findings of the LDA experiments, but would not be essential for publication. There are several journals that could be approached with these papers:

- Bioinspiration & Biomimetics,
- Experiments in Fluids,
- Journal of Fluid Mechanics,
- Physics of Fluids.

A list of potential conferences is presented below:

- ICATDL 2018 : 20th International Conference on Aerodynamics, Thrust, Drag and Lift (Paris, May 2018),
- ECCM - ECFD 2018 - European conference for computational fluid dynamics (Glasgow, June 2018),
- Lisbon 2018 international symposium on applications of laser and imaging techniques to fluid mechanics (Lisbon, July 2018).

References

- Bechert, D., Bruse, M., and Hage, W. (2000). Experiments with three-dimensional riblets as an idealized model of shark skin. *Experiments in fluids*, 28(5):403–412.
- Bechert, D., Bruse, M., Hage, W., Van der Hoeven, J. T., and Hoppe, G. (1997). Experiments on drag-reducing surfaces and their optimization with an adjustable geometry. *Journal of fluid mechanics*, 338:59–87.
- Bechert, D., Hoppe, G., and Reif, W.-E. (1985). On the drag reduction of the shark skin. In *1985 AIAA Shear Flow Control Conference*.
- Bixler, G. D. and Bhushan, B. (2013). Fluid drag reduction with shark-skin riblet inspired microstructured surfaces. *Advanced Functional Materials*, 23(36):4507–4528.
- Boomsma, A. (2015). *Drag Reduction by Riblets & Sharkske Denticles: A Numerical Study*. PhD thesis, University of Minnesota.
- Boomsma, A. and Sotiropoulos, F. (2016). Direct numerical simulation of sharkske denticles in turbulent channel flow. *Physics of Fluids*, 28(3):035106.
- Büttner, C. C. and Schulz, U. (2011). Shark skin inspired riblet structures as aerodynamically optimized high temperature coatings for blades of aeroengines. *Smart Materials and Structures*, 20(9):094016.
- Caram, J. and Ahmed, A. (1991). Effect of riblets on turbulence in the wake of an airfoil. *AIAA journal*, 29(11):1769–1770.
- Caretto, L., Gosman, A., Patankar, S., and Spalding, D. (1973). Two calculation procedures for steady, three-dimensional flows with recirculation. In *Proceedings of the third international conference on numerical methods in fluid mechanics*, pages 60–68. Springer.
- Chamorro, L. P., Arndt, R., and Sotiropoulos, F. (2013). Drag reduction of large wind turbine blades through riblets: Evaluation of riblet geometry and application strategies. *Renewable energy*, 50:1095–1105.
- Chen, H., Zhang, X., Ma, L., Che, D., Zhang, D., and Sudarshan, T. (2014). Investigation on large-area fabrication of vivid shark skin with superior surface functions. *Applied Surface Science*, 316:124–131.
- Choi, K.-S. (1990). Effects of longitudinal pressure gradients on turbulent drag reduction with riblets. In *Turbulence Control by Passive Means*, pages 109–121. Springer.

- Chu, D. C. and Karniadakis, G. E. (1993). A direct numerical simulation of laminar and turbulent flow over riblet-mounted surfaces. *Journal of Fluid Mechanics*, 250:1–42.
- Clauser, F. H. (1956). The turbulent boundary layer. *Advances in applied mechanics*, 4:1–51.
- Coustols, E. and Schmitt, V. (1990). Synthesis of experimental riblet studies in transonic conditions. In *Turbulence Control by Passive Means*, pages 123–140. Springer.
- Dean, B. and Bhushan, B. (2010). Shark-skin surfaces for fluid-drag reduction in turbulent flow: a review. *Philosophical Transactions of the Royal Society of London A: Mathematical, Physical and Engineering Sciences*, 368(1929):4775–4806.
- Debisschop, J. and Nieuwstadt, F. (1996). Turbulent boundary layer in an adverse pressure gradient-effectiveness of riblets. *AIAA journal*, 34(5):932–937.
- Díez, G., Soto, M., and Blanco, J. (2015). Biological characterization of the skin of shortfin mako shark *isurus oxyrinchus* and preliminary study of the hydrodynamic behaviour through computational fluid dynamics. *Journal of fish biology*, 87(1):123–137.
- Ferziger, J. H., Peric, M., and Leonard, A. (1997). Computational methods for fluid dynamics.
- Flack, K. A. and Schultz, M. P. (2010). Review of hydraulic roughness scales in the fully rough regime. *Journal of Fluids Engineering*, 132(4):041203.
- Fletcher, T., Altringham, J., Peakall, J., Wignall, P., and Dorrell, R. (2014). Hydrodynamics of fossil fishes. In *Proc. R. Soc. B*, volume 281, page 20140703. The Royal Society.
- Fletcher, T. M. (2015). *The Evolution of Speed: an empirical and comparative analysis of drag-reducing scales in early fishes*. PhD thesis, University of Leeds.
- Fukagata, K., Iwamoto, K., and Kasagi, N. (2002). Contribution of reynolds stress distribution to the skin friction in wall-bounded flows. *Physics of Fluids*, 14(11):L73–L76.
- García-Mayoral, R. and Jiménez, J. (2011). Drag reduction by riblets. *Philosophical Transactions of the Royal Society of London A: Mathematical, Physical and Engineering Sciences*, 369(1940):1412–1427.
- Garcia-Mayoral, R. and Jimenez, J. (2011). Hydrodynamic stability and breakdown of the viscous regime over riblets. *Journal of Fluid Mechanics*, 678:317–347.

- García-Mayoral, R. and Jiménez, J. (2012). Scaling of turbulent structures in riblet channels up to $Re_\tau = 550$. *Physics of Fluids*, 24(10):105101.
- Germano, M., Piomelli, U., Moin, P., and Cabot, W. H. (1991). A dynamic subgrid-scale eddy viscosity model. *Physics of Fluids A: Fluid Dynamics (1989-1993)*, 3(7):1760–1765.
- Goring, D. G. and Nikora, V. I. (2002). Despiking acoustic doppler velocimeter data. *Journal of Hydraulic Engineering*, 128(1):117–126.
- Grüneberger, R. and Hage, W. (2011). Drag characteristics of longitudinal and transverse riblets at low dimensionless spacings. *Experiments in Fluids*, 50(2):363–373.
- Han, M., Lim, H. C., Jang, Y.-G., Lee, S. S., and Lee, S.-J. (2003). Fabrication of a micro-riblet film and drag reduction effects on curved objects. In *TRANSDUCERS, Solid-State Sensors, Actuators and Microsystems, 12th International Conference on, 2003*, volume 1, pages 396–399. IEEE.
- Issa, R. I. (1986). Solution of the implicitly discretised fluid flow equations by operator-splitting. *Journal of computational physics*, 62(1):40–65.
- Jimenez, J. (2004). Turbulent flows over rough walls. *Annu. Rev. Fluid Mech.*, 36:173–196.
- Kasagi, N. and Fukagata, K. (2006). *The FIK identity and its implication for turbulent skin friction control*. World Scientific, Singapore.
- Kim, J., Moin, P., and Moser, R. (1987). Turbulence statistics in fully developed channel flow at low reynolds number. *Journal of fluid mechanics*, 177:133–166.
- Klumpp, S., Guldner, T., Meinke, M., and Schröder, W. (2010). Riblets in a turbulent adverse-pressure gradient boundary layer. In *5th Flow Control Conference*, page 4706.
- Lang, A. W., Bradshaw, M. T., Smith, J. A., Wheelus, J. N., Motta, P. J., Habegger, M. L., and Hueter, R. E. (2014). Movable shark scales act as a passive dynamic micro-roughness to control flow separation. *Bioinspiration & biomimetics*, 9(3):036017.
- Lee, S.-J. and Lee, S.-H. (2001). Flow field analysis of a turbulent boundary layer over a riblet surface. *Experiments in fluids*, 30(2):153–166.
- Lilly, D. K. (1992). A proposed modification of the germano subgrid-scale closure method. *Physics of Fluids A: Fluid Dynamics*, 4(3):633–635.
- Luchini, P., Manzo, F., and Pozzi, A. (1991). Resistance of a grooved surface to parallel flow and cross-flow. *Journal of fluid mechanics*, 228:87–109.

- Luo, Y., Liu, Y., Anderson, J., Li, X., and Li, Y. (2015a). Improvement of water-repellent and hydrodynamic drag reduction properties on bio-inspired surface and exploring sharkskin effect mechanism. *Applied Physics A*, 120(1):369–377.
- Luo, Y., Wang, J., Sun, G., Li, X., and Liu, Y. (2015b). Experimental investigations on manufacturing different-shaped bio-inspired drag-reducing morphologies and hydrodynamic testing. *Experimental Techniques*.
- Meneveau, C., Lund, T. S., and Cabot, W. H. (1996). A lagrangian dynamic subgrid-scale model of turbulence. *Journal of Fluid Mechanics*, 319:353–385.
- Menter, F., Kuntz, M., and Langtry, R. (2003). Ten years of industrial experience with the sst turbulence model. *Turbulence, heat and mass transfer*, 4(1):625–632.
- Menter, F. R. (1994). Two-equation eddy-viscosity turbulence models for engineering applications. *AIAA journal*, 32(8):1598–1605.
- Moser, R. D., Kim, J., and Mansour, N. N. (1999). Direct numerical simulation of turbulent channel flow up to $Re_\tau = 590$. *Phys. Fluids*, 11(4):943–945.
- Murthy, J. and Mathur, S. (1997). Periodic flow and heat transfer using unstructured meshes. *International journal for numerical methods in fluids*, 25(6):659–677.
- Neumann, D. and Dinkelacker, A. (1991). Drag measurements on v-grooved surfaces on a body of revolution in axial flow. *Applied Scientific Research*, 48(1):105–114.
- Newhall, K. A. (2006). *Turbulent boundary layers: a look at skin friction, pressure gradient, surface roughness and the power law*. PhD thesis, Rensselaer Polytechnic Institute.
- Nieuwstadt, F., Wolthers, W., Leijdens, H., Krishna Prasad, K., and Schwarz-van Manen, A. (1993). The reduction of skin friction by riblets under the influence of an adverse pressure gradient. *Experiments in fluids*, 15(1):17–26.
- Nikuradse, J. (1933). Laws of flow in rough pipes. In *VDI Forschungsheft*. Citeseer.
- Perlin, M., Dowling, D. R., and Ceccio, S. L. (2016). Freeman scholar review: Passive and active skin-friction drag reduction in turbulent boundary layers. *Journal of Fluids Engineering*, 138(9):091104.
- Pope, S. B. (2001). Turbulent flows.
- Reidy, L. W. and Anderson, G. W. (1988). Drag reduction for external and internal boundary layers using riblets and polymers. *AIAA Pap*, (88-0138).

- Reif, W.-E. (1985). *Squamation and ecology of sharks*. Senckenbergische Naturforschende Gesellschaft.
- Rhie, C. and Chow, W. L. (1983). Numerical study of the turbulent flow past an airfoil with trailing edge separation. *AIAA journal*, 21(11):1525–1532.
- Rohr, J., Andersen, G., Reidy, L., and Hendricks, E. (1992). A comparison of the drag-reducing benefits of riblets in internal and external flows. *Experiments in fluids*, 13(6):361–368.
- Sareen, A., Deters, R., Henry, S., and Selig, M. (2011). Paper# aiaa-2011-558. In *49th AIAA Aerospace Sciences Meeting, AIAA, Orlando, FL, New York*.
- Smagorinsky, J. (1963). General circulation experiments with the primitive equations: I. the basic experiment*. *Monthly weather review*, 91(3):99–164.
- Subaschandar, N., Kumar, R., and Sundaram, S. (1999). Drag reduction due to riblets on a gaw (2) airfoil. *Journal of aircraft*, 36(5):890–892.
- Sundaram, S., Viswanath, P., and Rudrakumar, S. (1996). Viscous drag reduction using riblets on naca 0012 airfoil to moderate incidence. *AIAA journal*, 34(4):676–682.
- Sundaram, S., Viswanath, P., and Subaschandar, N. (1999). Viscous drag reduction using riblets on a swept wing. *AIAA journal*, 37(7):851–856.
- Viswanath, P. and Mukund, R. (1995). Turbulent drag reduction using riblets on a supercritical airfoil at transonic speeds. *AIAA journal*, 33(5):945–947.
- Vreman, A. and Kuerten, J. (2014). Comparison of direct numerical simulation databases of turbulent channel flow at $Re_\tau = 180$. *Physics of Fluids*, 26(1):015102.
- Walsh, M. J. (1982). Turbulent boundary layer drag reduction using riblets. In *AIAA, Aerospace sciences meeting*, volume 1.
- Walsh, M. J. (1990). Effect of detailed surface geometry on riblet drag reduction performance. *Journal of Aircraft*, 27(6):572–573.
- Wen, L., Weaver, J. C., and Lauder, G. V. (2014). Biomimetic shark skin: design, fabrication and hydrodynamic function. *Journal of Experimental Biology*, 217(10):1656–1666.
- Wen, L., Weaver, J. C., Thornycroft, P. J., and Lauder, G. V. (2015). Hydrodynamic function of biomimetic shark skin: effect of denticle pattern and spacing. *Bioinspiration & Biomimetics*, 10(6):066010.
- Wetzel, K. K. and Farokhi, S. (1996). Interaction of riblets and vortex generators on an airfoil.

- Wilkinson, S. and Lazos, B. (1988). Direct drag and hot-wire measurements on thin-element riblet arrays. In *Turbulence Management and Relaminarisation*, pages 121–131. Springer.
- Yang, S.-Q., Li, S., Tian, H.-P., Wang, Q.-Y., and Jiang, N. (2016). Tomographic piv investigation on coherent vortex structures over shark-skin-inspired drag-reducing riblets. *Acta Mechanica Sinica*, 32(2):284–294.
- Zhang, D., Li, Y., Han, X., Li, X., and Chen, H. (2011a). High-precision bio-replication of synthetic drag reduction shark skin. *Chinese Science Bulletin*, 56(9):938–944.
- Zhang, D.-Y., Luo, Y.-H., Xiang, L., and Chen, H.-W. (2011b). Numerical simulation and experimental study of drag-reducing surface of a real shark skin. *Journal of Hydrodynamics, Ser. B*, 23(2):204–211.
- Zhang, Z. (2010). Lda application examples. In *LDA Application Methods*. Springer.
- Zhao, D.-Y., Huang, Z.-P., Wang, M.-J., Wang, T., and Jin, Y. (2012). Vacuum casting replication of micro-riblets on shark skin for drag-reducing applications. *Journal of Materials Processing Technology*, 212(1):198–202.

Appendix A: Pressure Coupling Methods

This section details the pressure coupling methods adopted in Sections 7 and 8. Both SIMPLE (Caretto et al., 1973) and PISO (Issa, 1986) algorithms can be derived from a semi-discrete form of the momentum equation:

$$\mathbf{a}_p \mathbf{U}_p = \mathbf{H} - \nabla P, \quad (40)$$

where \mathbf{a}_p represents the matrix coefficients of the velocity \mathbf{U}_p in the cell p . \mathbf{H} represents the explicit source terms and the influence from the neighbouring cells:

$$\mathbf{H} = - \sum_n \mathbf{a}_n \mathbf{U}_n + \mathbf{S}, \quad (41)$$

where subscript n represents the neighbours, and \mathbf{S} the source terms. The continuity equation is discretised as

$$\nabla \cdot \mathbf{U} = \sum_f \mathbf{S} \cdot \mathbf{U}_f = 0, \quad (42)$$

where \mathbf{S} denotes the outward pointing face area vector and subscript f denotes the face value. Face values are calculated by reformulating (40) for the cell faces, whereby the pressure gradient is evaluated from the neighbouring cells, as per Rhee and Chow (1983):

$$\mathbf{U}_f = \left(\frac{\mathbf{H}}{\mathbf{a}_p} \right)_f - \frac{(\nabla P)_f}{\mathbf{a}_{p,f}}. \quad (43)$$

By substituting \mathbf{U}_f into the continuity equation, (42), we form a Laplacian equation for pressure:

$$\nabla \cdot \left(\frac{(\nabla P)_f}{\mathbf{a}_{p,f}} \right) = \sum_f \mathbf{S} \cdot \left(\frac{\mathbf{H}}{\mathbf{a}_p} \right)_f. \quad (44)$$

The PISO algorithm (Issa, 1986) calculates the pressure and velocity fields in the following way:

1. Set initial conditions at $t = 0$.
2. Construct \mathbf{H} and solve the *momentum predictor* equation, (40), for the velocity field, using the pressure field from the previous known solution. This is known as the *pressure correction* step.
3. Update \mathbf{H} using the predicted velocity field and solve the pressure equation, (44), to update the pressure field.
4. Carry out a *velocity corrector* step by solving (40). Repeat steps 3 and 4 to ensure second order accuracy (Issa, 1986).

5. Exit the PISO loop and solve transport equations for other scalars (such as turbulent transport equations)
6. repeat for the next time step.

The reason for the corrector stage is to ensure the continuity equation is satisfied by the velocity field.

The steady-state SIMPLE algorithm (Caretto et al., 1973) adopts a similar approach to PISO, but corrects the velocity and pressure only once, to ensure continuity. In order to ensure stability, the pressure and velocity fields are relaxed. This method assumes that since a steady state solution is desired, the effect of not correcting the velocity field multiple times at step 3 will reduce computing costs at a reduction in convergence rate (Ferziger et al., 1997).

Appendix B: Notes on LES Closures

This section details the method of defining the sub-grid scale model for the dynamic large eddy simulation. A general filtering operator is defined by

$$\bar{U}_i(x_i, t) = \int G(r_i, x_i) U_i(x_i - r_i, t) dr_i, \quad (45)$$

where \bar{U}_i is the filtered velocity field, U_i is the velocity field, r_i is a radial coordinate, and $G(r_i, x_i)$ is the filtering operator. This work adopts a top-hat filter, whereby contributions to the filtered field are only taken if the radial coordinate lies within the filter width, $\bar{\Delta}$. The residual velocity is defined by

$$u'_i(x_i, t) \equiv U_i(x_i, t) - \bar{U}_i(x_i, t). \quad (46)$$

The residual pressure is defined in the same way. When the filtering operator is applied to the continuity and momentum equations we arrive at,

$$\frac{\partial \bar{U}_i}{\partial x_i} = 0, \quad (47)$$

and

$$\frac{\partial \bar{U}_i}{\partial t} + \frac{\partial \bar{U}_i \bar{U}_j}{\partial x_j} - \frac{\partial \bar{\sigma}_{ij}}{\partial x_j} = -\frac{\partial \bar{P}}{\partial x_i}. \quad (48)$$

The second term of the filtered momentum equation requires information about the unfiltered field in order to be evaluated. We therefore define a residual-stress tensor:

$$\tau_{ij}^R \equiv \tau_{ij}^r + \frac{1}{3} \tau_{kk}^R \delta_{ij} \equiv \bar{U}_i \bar{U}_j - \bar{U}_i \bar{U}_j, \quad (49)$$

where τ_{ij}^R is the residual stress tensor and τ_{ij}^r is its anisotropic component. When substituted into the momentum equation (48) we get,

$$\frac{\partial \bar{U}_i}{\partial t} + \frac{\partial \bar{U}_i \bar{U}_j}{\partial x_j} + \frac{\partial \tau_{ij}^r}{\partial x_j} - \frac{\partial \bar{\sigma}_{ij}}{\partial x_j} = -\frac{\partial \bar{P}}{\partial x_i}. \quad (50)$$

The residual stress is modelled using the closure of Smagorinsky (1963):

$$\tau_{ij}^r = -2(C_s \bar{\Delta})^2 |\bar{S}| \bar{S}_{ij}, \quad (51)$$

where C_s is the Smagorinsky constant, and \bar{S} and \bar{S}_{ij} are given by,

$$\bar{S}_{ij} = \frac{1}{2} \left(\frac{\partial \bar{U}_i}{\partial x_j} + \frac{\partial \bar{U}_j}{\partial x_i} \right), \quad |\bar{S}| = (2 \bar{S}_{ij} \bar{S}_{ij})^{1/2}. \quad (52)$$

The Smagorinsky constant is typically assigned a value of $C_s = 0.17$. The momentum equation, (50), can now be solved for the filtered velocity field by evaluating the residual stress using the fluid rate of strain. It should be noted that the filtering is implicit; the form of the filtering operator is not required to solve for the filtered field. However, the assumption that there is no dependence on space or time is a large limitation to the model. An alternative method, first proposed by Germano et al. (1991), involves filtering the momentum equations a second time in order to derive a relationship between C_s and the filtered velocity field:

$$\frac{\partial \tilde{U}_i}{\partial t} + \frac{\partial \widetilde{U_i U_j}}{\partial x_j} - \frac{\partial \tilde{\sigma}_{ij}}{\partial x_j} = -\frac{\partial \tilde{P}}{\partial x_i}, \quad (53)$$

where the second filtering operator is defined by

$$\tilde{U}_i(x_i, t) = \int \tilde{G}(r_i, x_i) U_i(x_i - r_i, t) dr_i. \quad (54)$$

The residual stress, based on the double-filtered equations, is defined as

$$T_{ij} \equiv T_{ij}^r + \frac{1}{3} T_{kk} \delta_{ij} \equiv \widetilde{U_i U_j} - \tilde{U}_i \tilde{U}_j. \quad (55)$$

Germano et al. (1991) related the once and twice-filtered residual stresses by subtracting them from one another, resulting in

$$L_{ij} \equiv L_{ij}^r + \frac{1}{3} L_{kk} \delta_{ij} \equiv T_{ij} - \widetilde{\tau_{ij}}^R = \widetilde{U_i U_j} - \tilde{U}_i \tilde{U}_j. \quad (56)$$

which does not require information from the unfiltered field in order to evaluate. By assuming T_{ij}^r can be modelled in the same way as τ_{ij}^r , we get

$$T_{ij}^r = -2(C_s \tilde{\Delta})^2 |\tilde{S}| \tilde{S}_{ij}, \quad (57)$$

where $\tilde{\Delta}$ is the filter width of the second filter. By using the Germano et al. (1991) identity, (56), we can define a relationship between L_{ij} and C_s :

$$L_{ij}^r = T_{ij}^r - \widetilde{\tau_{ij}}^r = C_s^2 M_{ij}, \quad M_{ij} = 2\tilde{\Delta}^2 |\tilde{S}| \widetilde{S}_{ij} - 2\tilde{\Delta}^2 |\tilde{S}| \tilde{S}_{ij}. \quad (58)$$

Since L_{ij} can be evaluated from the filtered velocity field, and M_{ij} can be evaluated from the filtered rate of strain, the only unknown in (58) is C_s^2 . However, this represents 5 equations with only one unknown. Lilly (1992) proposes a least squares method to reduce

the error associated with (58), resulting in

$$C_s^2 = \frac{L_{ij}M_{ij}}{M_{kl}M_{kl}}. \quad (59)$$

(59) can be used to close our system of equations by calculating C_s^2 for the residual stress of (51), which can then be used to evaluate the filtered momentum equation, (50). However, without spatial averaging and clipping, C_s^2 has a tendency to exhibit large fluctuations and negative (non-physical) values (Pope, 2001). In order to prevent this, the current work adopts the Lagrangian averaging technique of Meneveau et al. (1996).

$$C_s^2 = \frac{f_{LM}}{f_{MM}}, \quad (60)$$

where $f_{LM} = (L_{ij}M_{ij})_{ave}$ and $f_{MM} = (M_{ij}M_{ij})_{ave}$. Meneveau et al. (1996) construct a relaxation equation for these quantities:

$$\frac{\partial f_{LM}}{\partial t} + \frac{\partial}{\partial x_j}(\bar{U}_j f_{LM}) = \frac{1}{T}(L_{ij}M_{ij} - f_{LM}), \quad (61)$$

$$\frac{\partial f_{MM}}{\partial t} + \frac{\partial}{\partial x_j}(\bar{U}_j f_{MM}) = \frac{1}{T}(M_{ij}M_{ij} - f_{MM}). \quad (62)$$

where T is a specified relaxation time. These equations are equivalent to averaging along particle paths, with a relative weight $\exp[-(t - t')/T]$, where t' is the earlier time. The present work adopts a relaxation time of $T = 1.5\bar{\Delta}(f_{LM}f_{MM})^{-1/8}$, as recommended by Meneveau et al. (1996). Subsequently, the memory time is reduced in regions of high straining (high f_{MM}) and large nonlinear energy transfer (high f_{LM}). Although much less susceptible to negative values, f_{LM} is clipped in order to ensure physicality (positive C_s^2).

The procedure for closing the filtered momentum equation, by using the dynamic Lagrangian model of Meneveau et al. (1996), is as follows: We first calculated M_{ij} and L_{ij} using the once filtered, and twice filtered velocity field, from (56) and (58). These are then used to solve the relaxation equations, (61) and (62). This provides a value for the Smagorinsky constant, using (60), which is subsequently used to calculate the residual stress from (51). Lastly, the filtered momentum equation, (50), and the continuity equation, (47), can be solved for the filtered velocity and pressure field.